Title
Dispersion curve estimation via a spatial covariance method with ultrasonic wavefield imaging.

Authors
Chong, See Yenn
Todd, Michael D

Publication Date
2018-09-01

DOI
10.1016/j.ultras.2018.04.012

Peer reviewed

Dispersion Curve Estimation via a Spatial Covariance Method with Ultrasonic Wavefield Imaging

See Yenn Chong[a] and Michael D Todd[a,*]
[a]Department of Structural Engineering, University of California, 9500 Gilman Drive, La Jolla, San Diego, CA 92093, USA.
*Corresponding author: Email: mdtodd@mail.ucsd.edu Phone: +1(858)-534-5951

ABSTRACT

Numerous Lamb wave dispersion curve estimation methods have been developed to support damage detection and localization strategies in non-destructive evaluation/structural health monitoring (NDE/SHM) applications. In this paper, the covariance matrix is used to extract features from an ultrasonic wavefield imaging (UWI) scan in order to estimate the phase and group velocities of S0 and A0 modes. A laser ultrasonic interrogation method based on a Q-switched laser scanning system was used to interrogate full-field ultrasonic signals in a 2-mm aluminum plate at five different frequencies. These full-field ultrasonic signals were processed in three-dimensional space-time domain. Then, the time-dependent covariance matrices of the UWI were obtained based on the vector variables in Cartesian and polar coordinate spaces for all time samples. A spatial covariance map was constructed to show spatial correlations within the full wavefield. It was observed that the variances may be used as a feature for S0 and A0 mode properties. The phase velocity and the group velocity were found using a variance map and an enveloped variance map, respectively, at five different frequencies. This facilitated the estimation of Lamb wave dispersion curves. The estimated dispersion curves of the S0 and A0 modes showed good agreement with the theoretical dispersion curves.

Keywords: Ultrasonic wavefield imaging, laser ultrasonic, covariance matrix, covariance mapping, dispersion curves

1. INTRODUCTION

Ultrasonic Lamb waves are popular in non-destructive evaluation and structural health monitoring applications because they can offer an effective, relatively long range/area method to estimate the location, severity, and type of damage in structures. Lamb waves are dispersive and multimodal elastic waves that propagate along a plate of relatively small thickness. The dispersive profile of Lamb waves is typically characterized by phase and group velocity curves.

Many studies have employed Lamb waves dispersion curves themselves for damage detection and localization strategies [1-5]. Numerous group velocity measurement methods are introduced to improve the accuracy of the damage detection and localization. One of the methods, time-of-flight (ToF) measurement [6-11], has a rich history for group velocity estimation. Particularly, threshold crossing techniques [8, 10, 11] and temporal cross-correlation techniques [6, 9, 12] are typical methods for ultrasonic parameter extraction. A threshold crossing technique is a generalized approach and has been widely used to extract the ToF of a specific mode; specifically, the first arrival mode in most cases when the raw signal amplitude crosses a threshold. However, it shows less efficiency in estimating ToF when the monitoring mode is highly attenuated below the threshold. Therefore, a certain amount of prudence (and to some degree, non-quantitative judgment) is needed to define threshold level. The cross-correlation technique is another ToF measurement technique that estimates the arrival time difference by cross-correlating the amplitudes of two signals [6]. In general, the cross-correlation method is employed with the assumption that the response signal is only a shifted and scaled version of a reference signal with Gaussian white noise. However, when the measured signal in an experiment undergoes shape distortion, such as the dispersion of a propagating Lamb wave, then the time-based cross-correlation method may become less effective [9].

Besides these two techniques, signal decomposition techniques have also been introduced. One of the decomposition techniques is the time-frequency analysis (e.g. wavelet transform method). In the wavelet transform method, the ToF measurement may be performed since the peak of the magnitude of wavelet transform in the time–frequency domain is related to the arrival time of an ultrasonic wave signal of each frequency component [10, 11, 13-15]. In addition, the cross-correlation-based ToF measurement supplemented by wavelet transform was enhanced the accuracy of ToF estimation [16]. Another signal decomposition technique is the chirplet matching decomposition [9, 17], and it demonstrated better efficiency than the cross-correlation technique with acceptable error of around 2% [9]. A spectral decomposition technique was proposed [18, 19] as well to develop the group velocity curves of Lamb waves in an aluminum plate. The method enabled to reconstruct the dispersion curves of the fundamental modes with relative errors around 2%. However, the accuracy of the estimation method depended upon the bandwidth of the filter. Beyond ToF estimation methods, a model-based algorithm was proposed [20] to adaptively estimate Lamb waves dispersion curves using minimal a *priori* information and assumptions. Recently, phase array beamforming method [21] was proposed and demonstrated the ability to estimate group velocity curves for both isotropic and anisotropic materials.

Numerous methods have been investigated for phase velocity curve estimation as well. Typically, for the phase velocity measurement, ultrasonic signals are measured first using a pitch-catch method within a distance range from an/a excitation/sensor point and the measured signals are formed in a B-scan image; then, the time difference between the two-different fixed spatial points at the same ridge was determined for the phase velocity calculation of each mode, especially the fundamental Lamb wave modes. In time-domain analysis, the zero-crossing technique was proposed to estimate the time delay for the phase velocity measurement of S0 [22] and A0 [23] modes. The main idea of the technique was that using some threshold level the half period of the signal exceeding this level was determined. Then, the time instance at which the signal crosses the zero level was estimated. However, the accuracy of this technique depended upon the sampling frequency set during the signal acquisition process.

From the past decades, laser ultrasonic techniques (LUTs) have been under investigation and development for the inspection of mechanical engineering structures, as well as for phase velocities estimation [24, 25]. Then, in the current laser scanning technology, the experimental configuration setup of LUT for acquiring two-dimensional (2D) space domain is became simple and with high space resolution capability. With these advancements, B-scan data is easily obtained with high space resolution for the phase velocity estimation [26, 27]. Besides estimating the phase velocity directly from the B-scan data in the time-space domain, the phase velocity curves are estimated in an alternative form—frequency and wavenumber—by transforming the B-scan data from time-space domain to the frequency-wavenumber domain using two-dimensional Fourier transform method [28, 29]. Some studies also demonstrated that the LUTs incorporated with wavelet transform [10, 30] and statistical threshold estimation method [11] to measure ToF for group velocity estimation.

Since laser ultrasonic techniques provide high space resolution and large full-field ultrasonic data sets in three-dimensional (3D) space-time domain, a richer set of informative features may be extracted about the health condition of a structure. In the past decades, features extraction based on variance and/or covariance structure has been exploited, [31, 32]. This paper proposes a new approach based on spatial covariance to estimate phase and group velocities of S0 and A0 modes from full-field ultrasonic data. The computational burden of this proposed method is much lower than the spectral transformation methods. The covariance method is directly applied to the unprocessed "raw" measurement data, so there is no information loss on the spatial/temporal localization of features. Furthermore, the processing time needed for this proposed method is also shorter than the signal decomposition methods because the signal decomposition methods need preset dictionary elements to run iterative processing loops for results.

The following sections of this article will present the experimental setup for obtaining the full-field ultrasonic data using a laser ultrasonic generator, the theory and implementation of the covariance matrix for ultrasonic wavefield imaging, the analysis of the relationships between the spatial covariance matrix and the S0 and A0 mode waves, and the implementation of the variance map and the enveloped variance map for the phase and group velocities estimation.

2. EXPERIMENTAL SETUP

Figure 1(a) shows a schematic diagram of a laser ultrasonic interrogation system, which consists of a laser interrogator, a signal conditioning device, a data acquisition (DAQ) module, a contact sensor, and a computer used for operation control and signal processing. The laser scanning system consists of a 2D laser mirror scanner and a diode-pumped solid-state Q-switched Nd:YAG laser with 527 nm wavelength. In this paper, a 2-mm thick aluminum plate was setup at a standoff distance of 1780 mm from the 2D laser mirror scanner. Figures 2(a) and (b) show the theoretical phase velocity and group velocity curves of the two fundamental Lamb waves modes—the antisymmetric A0 mode and the symmetric S0 mode—for the 2-mm thickness aluminum plate. The dispersion curves were calculated with the commercial software (Vallen Dispersion) at the longitudinal wave velocity and shear wave velocity of 6320 m/s and 3100 m/s. In this paper, five different frequencies, 100, 150, 200, 300, and 400 kHz were considered to develop these dispersion curves.

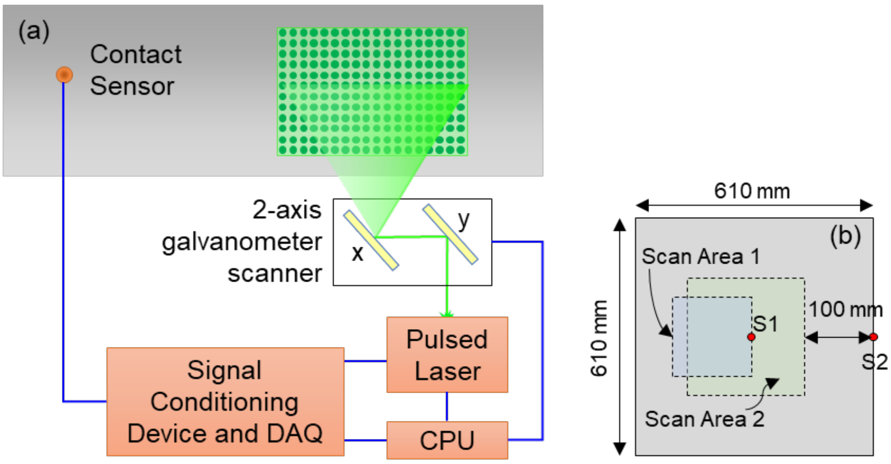

Figure 1. (a) Laser ultrasonic interrogation system configuration and (b) inspection configuration of a 2-mm aluminum plate.

Figure 1(b) shows two different configurations of scanning areas on the aluminum plate. First, the area of 200 mm × 200 mm was scanned with a scan interval of 1 mm for the frequency point of 400 kHz using a PZT sensor (S1) that was mounted at the center plate using cyanoacrylate adhesive. The laser scanning process was performed at an average pulse energy of 1 mJ (fluence of 23 mJ/cm^2) and the pulse repetition rate (PRR) was set to 20 Hz to avoid reverberation interference during the scanning process. The generated ultrasound was received and conditioned in an in-line bandpass filter through the PZT sensor. To obtain the dispersion curves at the frequency of 400 kHz, the bandpass filter was set at the center frequency of 400 kHz with the bandwidth of ±10 kHz. Subsequently, the filtered ultrasound was digitized in the DAQ module as shown in Fig. 1(a). The DAQ module was set with a sampling of T_s = 0.2 μs and K = 1000 total sample points. Once the scanning process was completed, the ultrasound in 2-D space with N and M grid points on the target were generated and formed in a 3D N by M by K space, indexed by spatial x-direction, spatial y-direction, and time t, respectively, along each dimension as shown in the left side of Fig. 3(a), named as ultrasonic wavefield imaging. Next, the experiment was repeated with the same configuration and the scanning process was performed separately for the UWI at different frequencies of 200 and 300 kHz respectively.

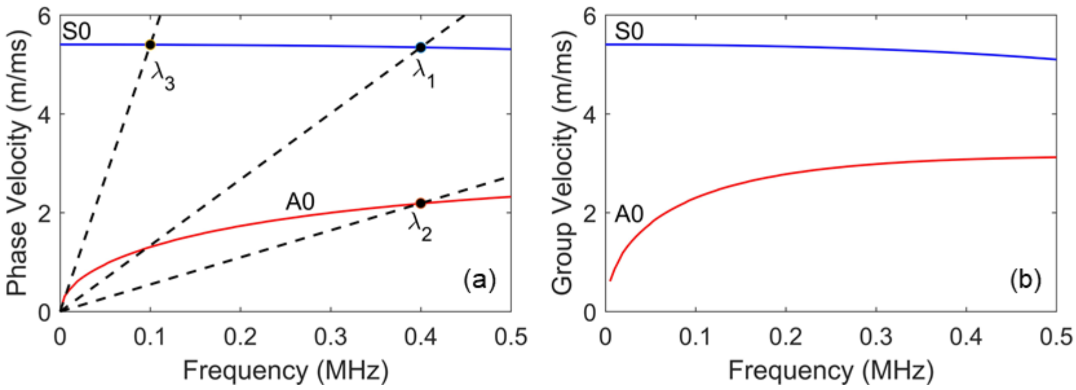

Figure 2. Theoretical (a) phase velocity and (b) group velocity curves of the two fundamental Lamb waves (A0 and S0 modes) of a 2-mm thick aluminum plate.

As shown in the phase velocity curves (Fig. 2(a)), the wavelengths of the S0 and A0 modes get longer at lower frequency. For the experimental setup in this paper, it was determined that the corresponding wavelength (λ_3 = 53 mm) of S0 mode at the frequency point of 100 kHz is the longest wavelength as compared to the other frequency. Henceforth, to allow S0 mode waves with 100 and 150 kHz to develop completely in the wavefield, the second scanning area was set to 300 mm × 300 mm as shown in Fig. 1(b). The experiment was performed with the same experimental setup as stated above, except that the sensor S1 was removed and reallocated, denoted as S2, at the edge of the plate, 100 mm away from the scanning area, as shown in Fig. 1(b). The center frequencies of the bandpass filter were set to 100 and 150 kHz respectively, to obtain the UWIs as desired for this experiment. The UWIs generated for each respective frequency will be used to estimate the dispersion curves via the proposed method. In this paper, ten sets of UWI at each frequency were generated to evaluate the reliability and precision of the proposed statistical method.

3. THE COVARIANCE MATRIX FOR ULTRASONIC WAVEFIELD IMAGING

Covariance (as a linear dispersion estimator) is defined as the mean value of the product of the standard deviations of two variables from their respective means. When it comes to a two-dimensional covariance problem, it may be expressed as a covariance matrix. Figure 3(a) shows that the 2D spatial waves of the S0 and A0 modes propagate as time progresses in the UWI; however, it does not show how the spatial local waves interact with or correlate to each other in the wavefield. Since the covariance method is principally used to learn the correlation among the variable vectors of a data set, it reveals the characteristics of the spatial correlation among the local waves at each instant in time. Consequently, it is hypothesized that the phase and group velocities of S0 and A0 modes waves may be estimated via the change of the spatial correlation response at a local point for a given time range. In this section, the covariance matrix of an UWI is studied to analyse the interaction (or unscaled correlation) of the ultrasonic wave responses between the two spatial samples of a spatial direction in Cartesian coordinate space, as well as polar coordinate space, as time evolves. Then, the diagonal of the covariance matrix (the variance) is extracted and its relationship to the Lamb waves is analyzed as well.

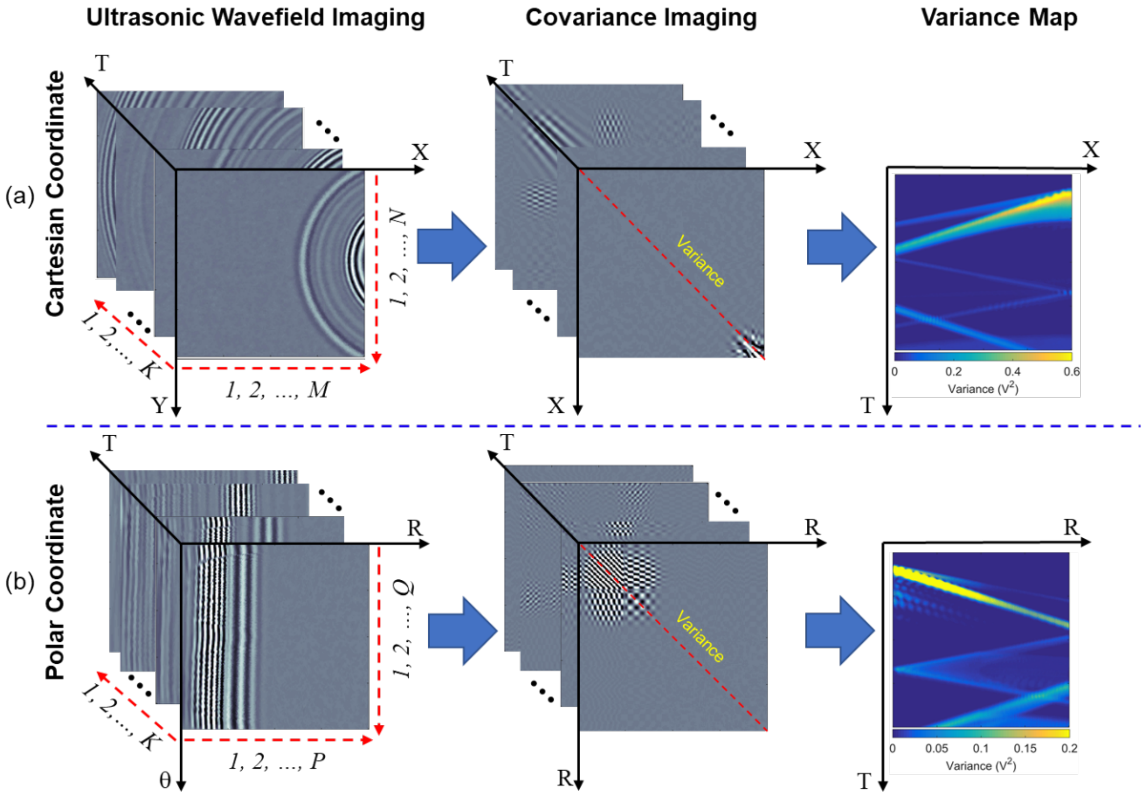

Figure 3. Overview of variance map generation based on ultrasonic wavefield imaging in (a) Cartesian coordinate and (b) polar coordinate spaces

3.1 Cartesian Coordinate Space

Figure 3(a) shows the generation of a spatial covariance image and subsequent variance map based on an UWI along T-axis in the Cartesian coordinate space. The covariance imaging is generated by calculating the covariance matrix of 2-D spatial ultrasonic wavefield imaging for each time-index k and the integer index k is in relation of time sample $t = kT_s$ in T-axis. Since the ultrasonic wavefield imaging for each time-index k is formed in $N \times M$ matrix as shown in the left side of Fig. 3(a), the elements of the $N \times M$ matrix are ultrasonic amplitudes in space domain and grouped into two random vectors, column vector and row vector. In X-axis, the column vector $\mathbf{X}_m$ is formed and m is an index that assigns a number to each spatial sample x with relation of $x = [(m-1) - M]\Delta x$, ranging from 1 to M in x-direction, as shown in Fig. 4(a). In Y-axis, the row vector $\mathbf{Y}_n$ is formed and n is an index that assigns a number to each spatial sample y with relation of $y = [(n-1) - N/2]\Delta y$, ranging from 1 to N in y-direction, as shown in Fig. 4(b). Then, Δx and Δy are the spatial sample interval (scan interval) for X- and Y-axes respectively. In this paper, both spatial sample intervals were set to 1 mm and M and N were set to 200 for the scan area 1 (200 mm × 200 mm) and 300 for the scan area 2 (300 mm × 300 mm) as shown in Fig. 1(b), respectively.

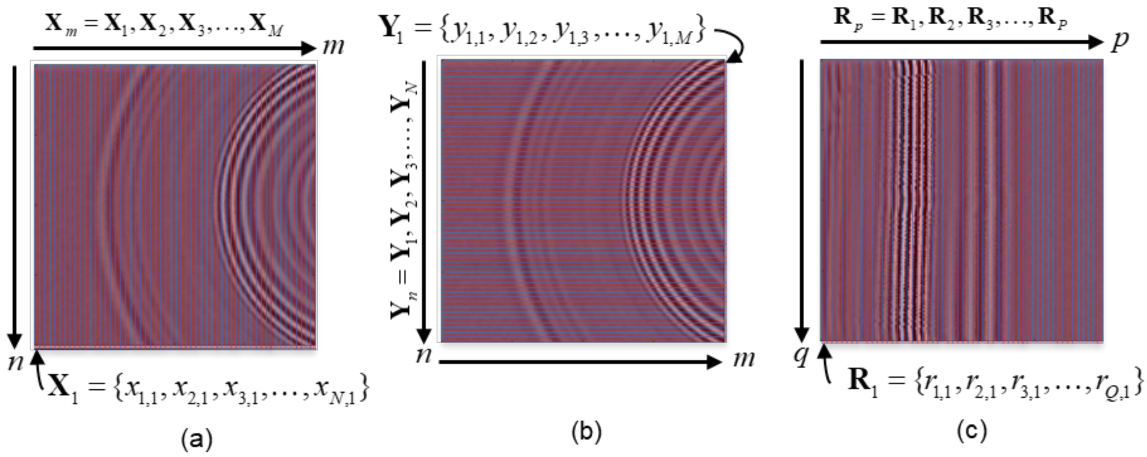

Figure 4. Assignments of column vectors of (a) $\mathbf{X}_m$, (b) $\mathbf{Y}_n$, and (c) $\mathbf{R}_p$ for ultrasonic wavefield imaging in Cartesian coordinate and polar coordinate spaces respectively.

For the covariance matrix of $\mathbf{X}_m$, M column vectors are considered in the covariance matrix calculation. As shown in Fig. 4(a), $\mathbf{X}_m = \{x_{1,m}, x_{2,m}, \ldots, x_{N,m}\}$ is a column vector with a set of ultrasonic amplitude values (denoted as $x_{n,m}$) in spatial samples with the index n ranging from 1 to N along Y-axis. The covariance matrix of $\mathbf{X}_m$ at a time-index is denoted as $\mathbf{C}_\mathbf{X}$ and expressed below:

$$\mathbf{C}_\mathbf{X} = \begin{pmatrix} c_{1,1}^\mathbf{X} & c_{1,2}^\mathbf{X} & \cdots & c_{1,M}^\mathbf{X} \\ c_{2,1}^\mathbf{X} & c_{2,2}^\mathbf{X} & \cdots & c_{2,M}^\mathbf{X} \\ \vdots & \vdots & \ddots & \vdots \\ c_{M,1}^\mathbf{X} & c_{M,2}^\mathbf{X} & \cdots & c_{M,M}^\mathbf{X} \end{pmatrix} \tag{1}$$

and the elements of $\mathbf{C}_\mathbf{X}$ are defined as:

$$c_{ij}^\mathbf{X} = \frac{1}{N-1}\sum_{n=1}^{N}\left(x_{n,i} - \bar{X}_i\right)\left(x_{n,j} - \bar{X}_j\right) \tag{2}$$

with the indices $i, j = 1, 2, \ldots, M$. The $\bar{X}_i$ and $\bar{X}_j$ are the mean of column vector $\mathbf{X}_m$. Since the covariance matrix in Eqn. (1) is a symmetric matrix with the matrix size of $M \times M$, for $i = j$ the diagonal elements ($c_{ii}^\mathbf{X}$) contain the variances, denoted as $\mathrm{var}_\mathbf{X}(m)$, of column vector $\mathbf{X}_m$; and for $i \neq j$

the off-diagonal elements contain the covariances between all possible pairs of column vector $\mathbf{X}_m$. Based on Eqn. (1), the covariance matrix of the 2-D spatial ultrasonic wavefield imaging for all the time-index k is calculated and denoted as $\mathbf{C}_\mathbf{X}(i,j,k)$. Lastly, the covariance matrix $\mathbf{C}_\mathbf{X}(i,j,k)$ is formed as covariance imaging as shown in the center of Fig. 3(a).

As for the covariance matrix of $\mathbf{Y}_n$, the matrix $N \times M$ of the ultrasonic wavefield imaging (Fig. 4(b)) is transposed first and yielded a column vector $\mathbf{Y}_n^T = \{y_{1,n}, y_{2,n}, \ldots, y_{M,n}\}$ with a set of ultrasonic amplitude values (denoted as $y_{m,n}$) in spatial samples (Fig. 4(b)). Hence, the elements of the covariance matrix of $\mathbf{Y}_n$ is defined as below:

$$c_{ij}^{\mathbf{Y}} = \frac{1}{M-1}\sum_{m=1}^{M}\left(y_{m,i} - \overline{Y}_i\right)\left(y_{m,j} - \overline{Y}_j\right) \tag{3}$$

And $i, j = 1, 2, \ldots, N$. The $\overline{Y}_i$ and $\overline{Y}_j$ are the means of column vector $\mathbf{Y}_n^T$. Since the covariance matrix is a symmetric matrix ($N \times N$), for $i = j$ the diagonal elements ($c_{ii}^{\mathbf{Y}}$) contain the variances, denoted as $\mathrm{var}_\mathbf{Y}(n)$, of column vector $\mathbf{Y}_n^T$; and for $i \neq j$ the off-diagonal elements estimate the covariances between all possible pairs of column vector $\mathbf{Y}_n^T$. For that, the covariance matrix of the 2D spatial ultrasonic wavefield imaging is calculated for all the time-index k and denoted as $\mathbf{C}_\mathbf{Y}(i,j,k)$. Lastly, the covariance matrix $\mathbf{C}_\mathbf{Y}(i,j,k)$ is referred to as a covariance image.

3.2 Polar Coordinate Space

Figure 3(b) shows the UWI in polar coordinate with R-, θ-, and T-axes, which are generated by transforming the UWI in Cartesian coordinate space based on the expression below:

$$r = \sqrt{x^2 + y^2} \text{ and } \theta = \tan^{-1}\left(\frac{y}{x}\right) \tag{4}$$

where, x and y are the spatial samples of the X- and Y-axes of the UWI. The r and θ are the spatial radius and circumferential angle, with the indices of p and q, respectively. The index p is assigned as a number to each spatial radius sample with the relation $r = (p-1)\Delta r$, ranging from 1 to P; and, the index q is assigned as number to each circumferential angle with the relation $\theta = \left[(q-1) - Q/2\right]\Delta\theta$, ranging from 1 to Q. In this paper, the radius interval Δr was set to 1 mm and P was set to 200 for the scan area 1 (200 mm × 200 mm) and 300 for the scan area 2 (300 mm × 300 mm) as shown in Fig. 1(b). The sensor point was set as the origin of the radius. The circumferential angle ranging was set from −30° to 30°. A simple linear interpolation process was performed with the Q = 120 on the results obtained from Eqn. (4) in order to obtain the angle interval of $\Delta\theta = 0.5°$ for the circumferential angle range.

In Fig. 3(b), each time-index of the UWI is formed in $Q \times P$ matrix and the elements are ultrasonic amplitude values as shown in Fig. 4(c). The elements are grouped into a random vector, column vector $\mathbf{R}_p$ with the total of P column vectors for the covariance matrix calculation. As shown in Fig. 4(c), $\mathbf{R}_p = \{r_{1,p}, r_{2,p}, \ldots, r_{Q,p}\}$ is a column vector with a set of ultrasonic amplitude values (denoted as $r_{q,p}$) in the circumferential angles with the index q ranging from 1 to Q along θ-axis, as shown in Fig. 4(c). The covariance matrix of $\mathbf{R}_p$ is determined in the same manner of the covariance matrix $\mathbf{C}_\mathbf{X}$ in Eqn. (1), and it is denoted as $\mathbf{C}_\mathbf{R}$ with the elements below:

$$c_{ij}^{\mathbf{R}} = \frac{1}{Q-1}\sum_{q=1}^{Q}\left(r_{q,i} - \overline{R}_i\right)\left(r_{q,j} - \overline{R}_j\right), \tag{5}$$

where, $i, j = 1, 2, \ldots, P$. The $\overline{R}_i$ and $\overline{R}_j$ are the means of column vector $\mathbf{R}_p$. Since the covariance matrix in Eqn. (5) is a symmetric matrix with the matrix size of $P \times P$, for $i = j$ the diagonal elements, denoted as $c_{ii}^{\mathbf{R}}$, contain the variances, denoted as $\mathrm{var}_\mathbf{R}(p)$, of column vector $\mathbf{R}_p$; and for $i \neq j$ the off-diagonal elements contain the covariance between all possible pairs of column vector $\mathbf{R}_p$. The process of determining the covariance matrix is executed for all the time indices to generate the covariance image, denoted as $\mathbf{C}_\mathbf{R}(i, j, k)$, as shown in the center of Fig. 3(b).

Lastly, the variance maps $\mathrm{var}_\mathbf{X}(m,k)$, $\mathrm{var}_\mathbf{Y}(n,k)$, and $\mathrm{var}_\mathbf{R}(p,k)$ were generated by mapping each variances of covariance matrices $\mathbf{C}_\mathbf{X}(i, j, k)$, $\mathbf{C}_\mathbf{Y}(i, j, k)$, and $\mathbf{C}_\mathbf{R}(i, j, k)$ for all k into 2D array matrix forms, represented in X-T plane and Y-T for Cartesian coordinate space and in R-T plane for polar coordinate space, as shown in Figs. 5(a-c) respectively.

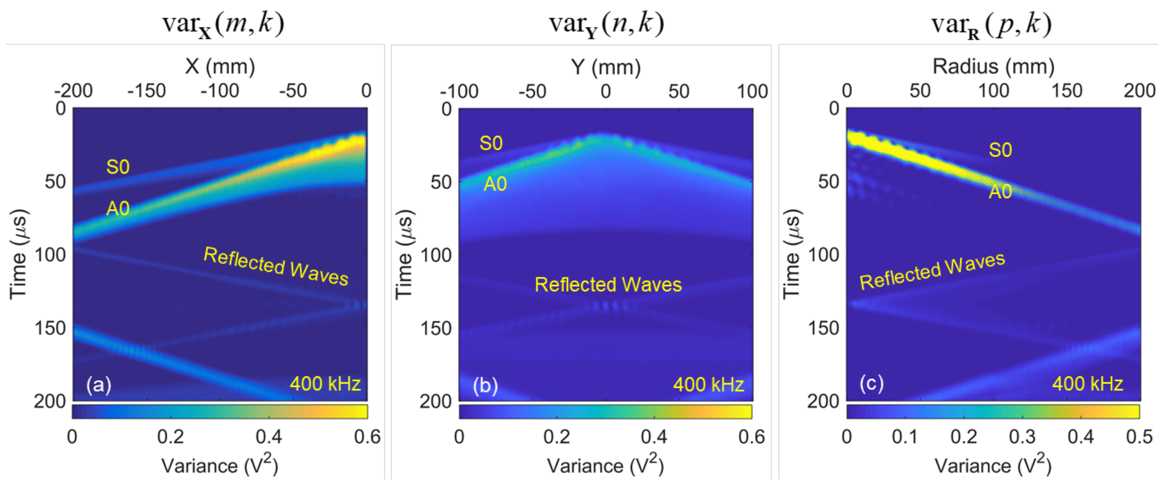

Figure 5. Variance maps based on the covariance matrices (a) $\mathbf{C}_{\mathbf{X}}(i,j,k)$, (b) $\mathbf{C}_{\mathbf{Y}}(i,j,k)$, and (c) $\mathbf{C}_{\mathbf{R}}(i,j,k)$.

3.3 Relationships between UWI and Covariance Imaging

Next, the relationships between UWI and covariance imaging are analyzed. The UWI used later for the discussion was obtained from the experiment as explained in previous section. To ease the analysis discussion, the ultrasonic wavefield image and the covariance image at a time sample of 40 μs ($k = 200$) with 400 kHz were considered for Cartesian and polar coordinate spaces.

Figures 6(a) and (b) show the UWI with 400 kHz at the time 40 μs and the corresponding covariance image $\mathbf{C}_{\mathbf{X}}(i,j,200)$, respectively, in Cartesian coordinate space. Based on the reciprocity of ultrasonic propagation [33], the omnidirectional ultrasonic waves were omitted from the sensor, located at (0,0), as shown in the wavefield image (Fig. 6(a)). The Lamb waves, S0 and A0 modes, were clearly visible in the ultrasonic wavefield image (Fig. 6(a)) at the first arrival distances of −140 mm (shaded blue-line) and −85 mm (shaded black-line), respectively. Figure 6(b) shows that the covariance image was symmetry along the diagonal line (shaded red-line). The diagonal values were the variances in relative to the spatial samples of X-axis and plotted in the inset of Fig. 6(b). Then, each off-diagonal element of $\mathbf{C}_{\mathbf{X}}(i,j,200)$ described the degree to which two spatial signals tended to correlate to each other.

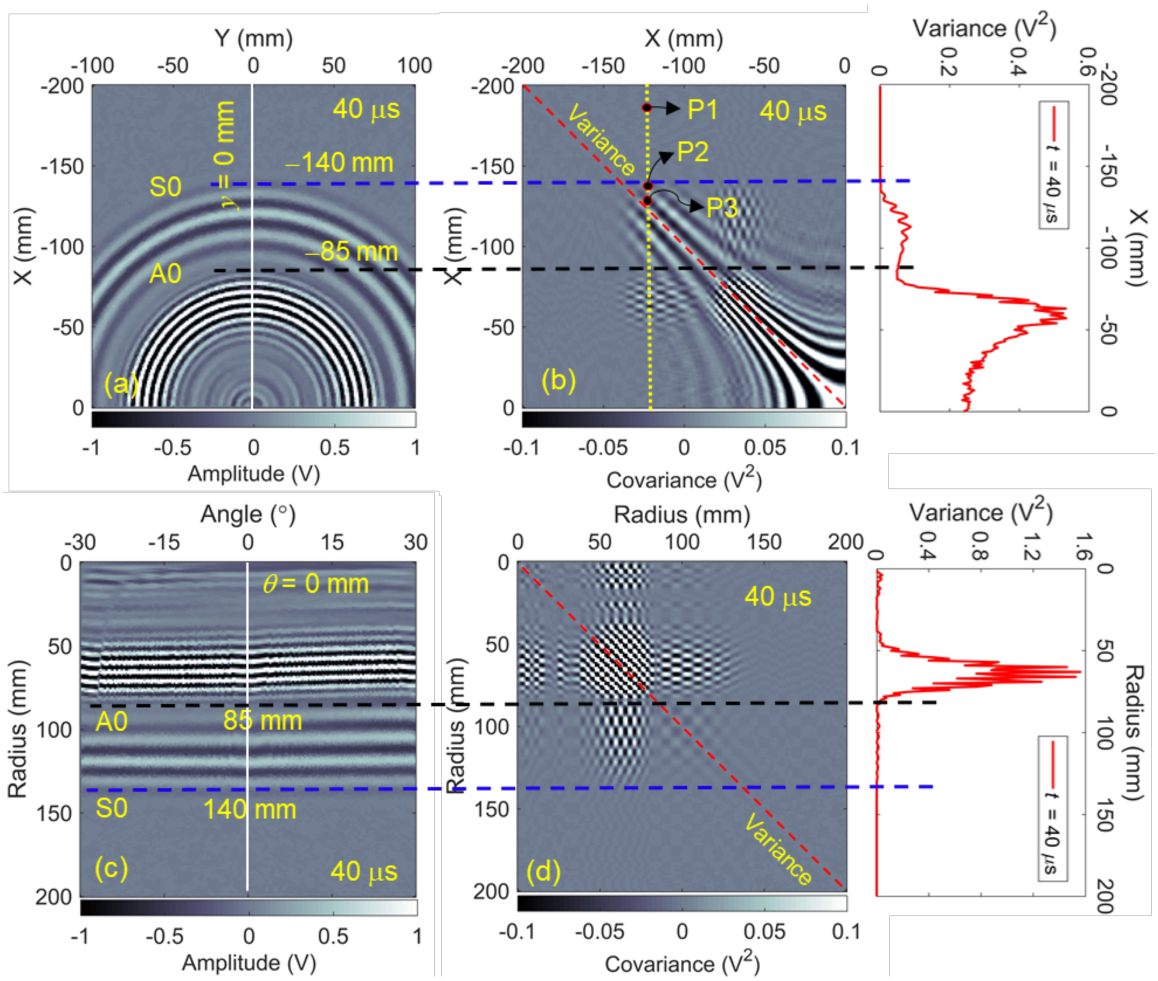

Figure 6. Cartesian coordinate space: (a) ultrasonic wavefield image and (b) its corresponding covariance image (inset: variance signal), and polar coordinate space: (c) ultrasonic wavefield imaging and (d) its corresponding covariance image (inset: variance signal), at 40 μs.

Figure 7(a) shows the covariance responses between the spatial signal $\mathbf{X}_{m=81}$ and $\mathbf{X}_m$ for m = 1, 2, …, 200. Since m and j were same in Eqn. (2), the index of j = 81 was referred to $\mathbf{X}_{m=81}$ and the corresponding spatial signal was at x = –120 mm. In Fig. 6(b), the covariances at the points of P1, P2, and P3 along a shaded yellow-line x = –120 mm were obtained based on the spatial signals at x = –120 mm ($\mathbf{X}_{m=81}$) with x = –180 mm ($\mathbf{X}_{m=21}$), with x = –133 mm ($\mathbf{X}_{m=68}$), and with x = –126 mm ($\mathbf{X}_{m=75}$) respectively and the respective covariances were shown in Fig. 7(a). Figure 7(b) shows the two spatial signals at x = –120 mm and x = –180 mm obtained from UWI in Fig. 6(a). The spatial signal at –180 mm showed as noise floor in Fig. 6(a) at 40 μs and the spatial signal at –120 mm showed the dominant energy in S0 mode wave. Hence, using Eqn. (2), the covariance of both spatial signals was determined to be zero at P1 as shown in Fig. 7(a), which indicates both signals are uncorrelated. For x = –120 mm with x = –133 mm, both signals were in similar wave pattern (in-phase) and yield positive covariance at P2. On the other hand, when $x = -126$ mm is out-of-phase to the $x = -120$ mm (Fig. 7(c)), the negative covariance was obtained at P3 as shown in Fig. 7(a). The values of the covariance elements indicated the degree to which two spatial signals tended to correlate to each other spatially.

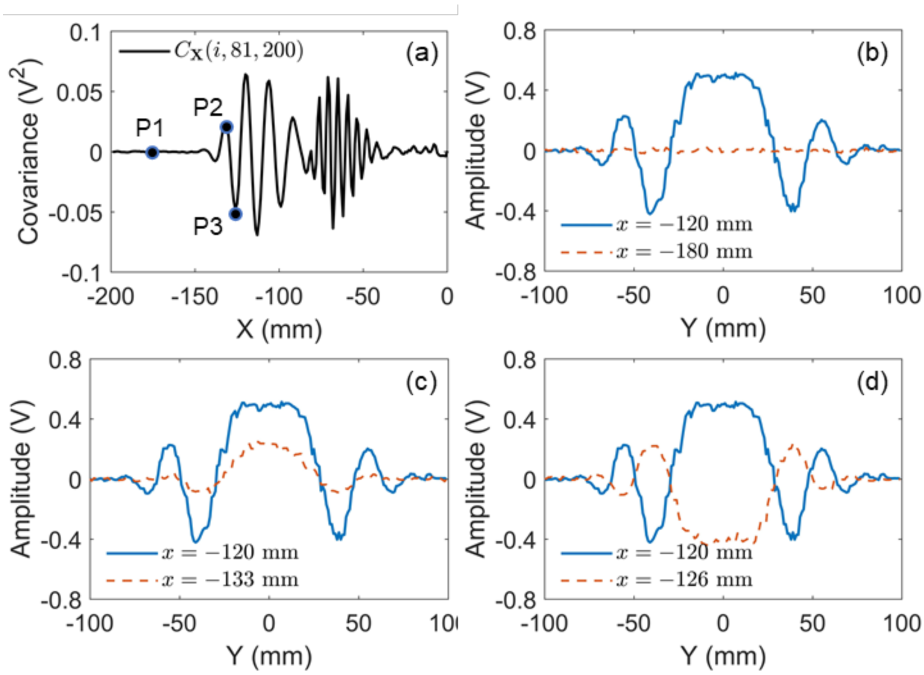

Figure 7. (a) Covariance responses between the spatial signal $\mathbf{X}_{m=81}$($x = -120$ mm) and $\mathbf{X}_m$ for all m; and the spatial signals of UWI at (b) $x = -180$ mm, (c) $x = -133$ mm, and (d) $x = -126$ mm in comparison to $x = -120$ mm.

Two distinguishable covariance responses were observed in -140 mm $< x < -85$ mm and -85 mm $< x < -50$ mm as shown in Fig. 6(b) and relationship to the S0 mode and A0 mode in Fig. 6(a) respectively. The corresponding variance signal (the inset of Fig. 6(b)) showed two wave packets with multiple peaks in both ranges. The variance signal indicated that the first arrival distances of the wave packets estimated at $x = -140$ mm and at $x = -85$ mm were approximately same as the first arrival distances of the S0 and A0 modes in Fig. 6(a), respectively.

Figure 8(a) shows the waveform of the ultrasound along spatial sample x at $y = 0$ mm in Fig. 6(a) with the peaks and troughs amplitudes of S0 mode (–133 mm, –126 mm, –120 mm) and A0 mode (–72 mm, –69 mm, –66 mm). Based on the peaks and throughs obtained in these S0 and A0 modes, the wavelengths of these S0 and A0 modes were determined at 13 mm and 6 mm based on the two consecutive peak locations (–120 mm and –133 mm) and (–66 mm and –72 mm), respectively.

Figures 8(b) and (c) show the zoomed first and second wave packets of the variance signal in the inset of Fig. 6(b). The peak locations of the zoomed first and second wave packets of the variance signal indicated that have the same peaks and troughs locations in the S0 and A0 mode waves in Fig. 8(a).

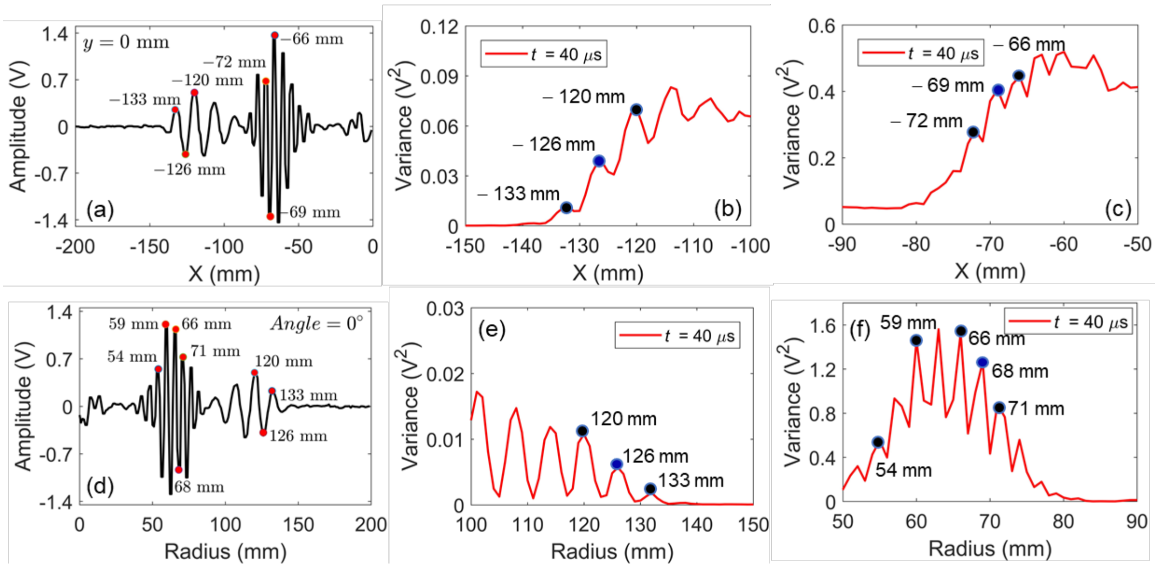

Figure 8. (a) Spatial signal at $y = 0$ mm of UWI in Fig. 6(a) and the zoomed (b) first and (c) second wave packets of the variance signal of $\mathbf{C}_\mathbf{X}$; and (d) spatial signal at $\theta = 0°$ of UWI in Fig. 6(c) and the zoomed (e) first and (f) second wave packets of the variance signal of $\mathbf{C}_\mathbf{R}$.

Regards to this, the variance signal demonstrated association to the S0 and A0 modes. Thereupon, the wavelengths of the Lamb wave modes may be estimated based on the location of the peaks in a variance signal, as an alternative approach to estimate the wavelengths of Lamb wave modes. Based on the peaks locations of the variance signal in Figs. 8(b) and (c), the wavelengths of the S0 and A0 modes were estimated at 13 mm and 6 mm with the wavelength deviation errors of 2.3 % and 11% in comparison to the theoretical wavelengths of $\lambda_1 = 13.3$ mm and $\lambda_2 = 5.4$ mm obtained from the phase velocity curves (Fig. 2(a)) at the frequency of 400 kHz.

Next, the covariance matrix calculation based on $\mathbf{Y}_n^T$ is considered. Figures 9(a) and (b) show the UWI at 40 μs and the corresponding covariance image obtained from Eqn. (3), respectively. The covariance image of $\mathbf{C}_\mathbf{Y}(i, j, 200)$ showed an "X"-pattern which was different from the covariance image of $\mathbf{C}_\mathbf{X}(i, j, 200)$ in Fig. 6(b). This is because of the symmetry in the ultrasonic wavefield (Fig. 9(a)) at $y = 0$ mm, where any two arbitrary spatial signals in $\mathbf{Y}_n^T$ taken for the covariance calculation were similar to each other (e.g. one spatial signal at $y = -50$ mm ($\mathbf{Y}_{n=51}^T$) and the other spatial signal at

y = 50 mm ($\mathbf{Y}_{n=151}^{T}$)). The inset of Fig. 9(b) shows also that the corresponding variance signal was symmetry as different from the variance signal of $\mathbf{C}_{\mathbf{X}}(i, j, 200)$.

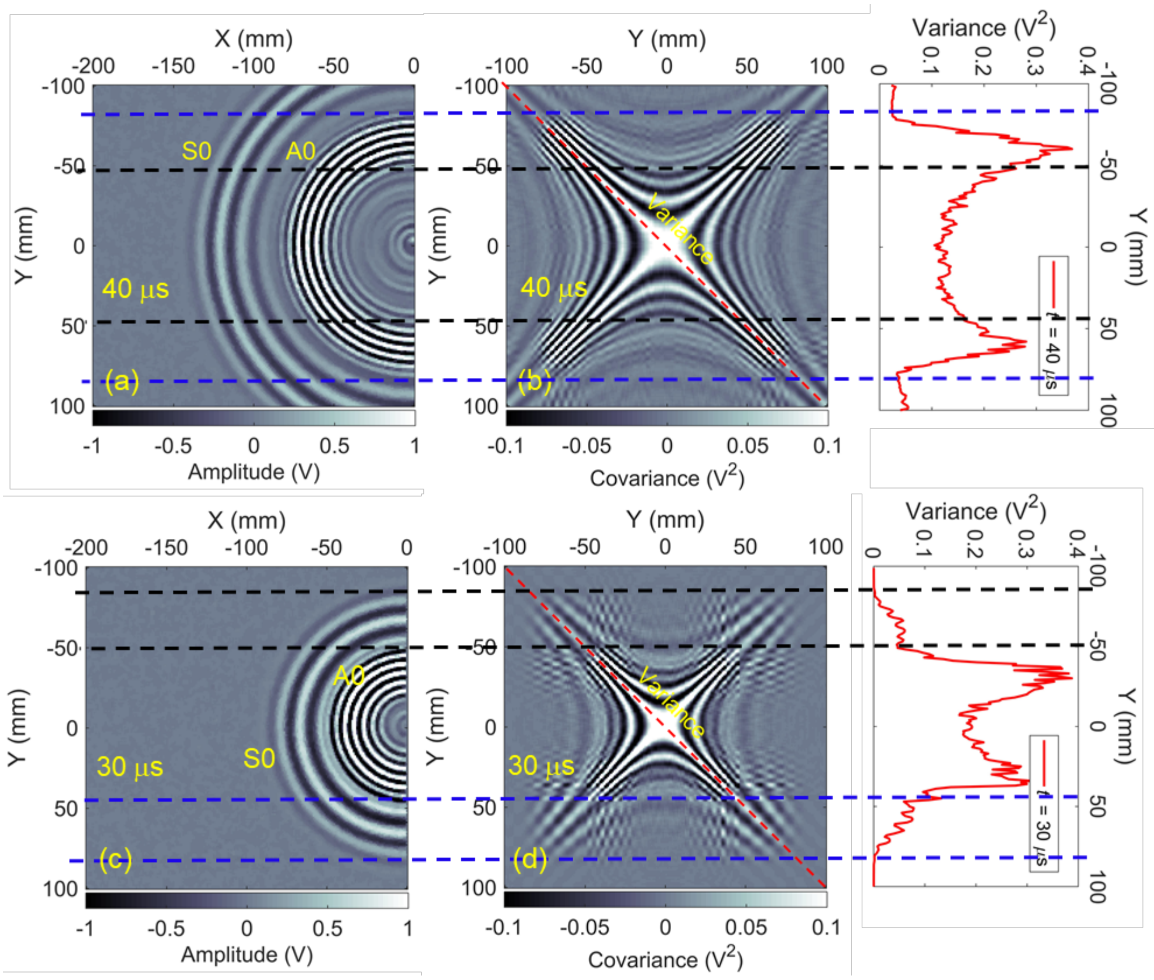

Figure 9. Cartesian coordinate space: Ultrasonic wavefield image and its corresponding covariance image (inset: variance signal) at (a)(b) 40 μs and (c)(d) 30 μs for $\mathbf{Y}_{n}^{T}$.

Figures 10(a) and (b) show the zoomed first and second wave packets of the variance signal in the inset of Fig. 9(b), and the peaks locations of (–71 mm, –68 mm, –66 mm) and (64 mm, 67 mm, 70 mm) showed same to the peaks locations of the A0 mode (–72 mm, –69 mm, –66 mm) in Fig. 8(a). Both peaks locations showed that the wavelengths were determined at 5 mm and 6 mm with the relative errors of 7.4% and 11% to the theoretical wavelength of A0 mode (λ_2 = 5.4 mm) respectively.

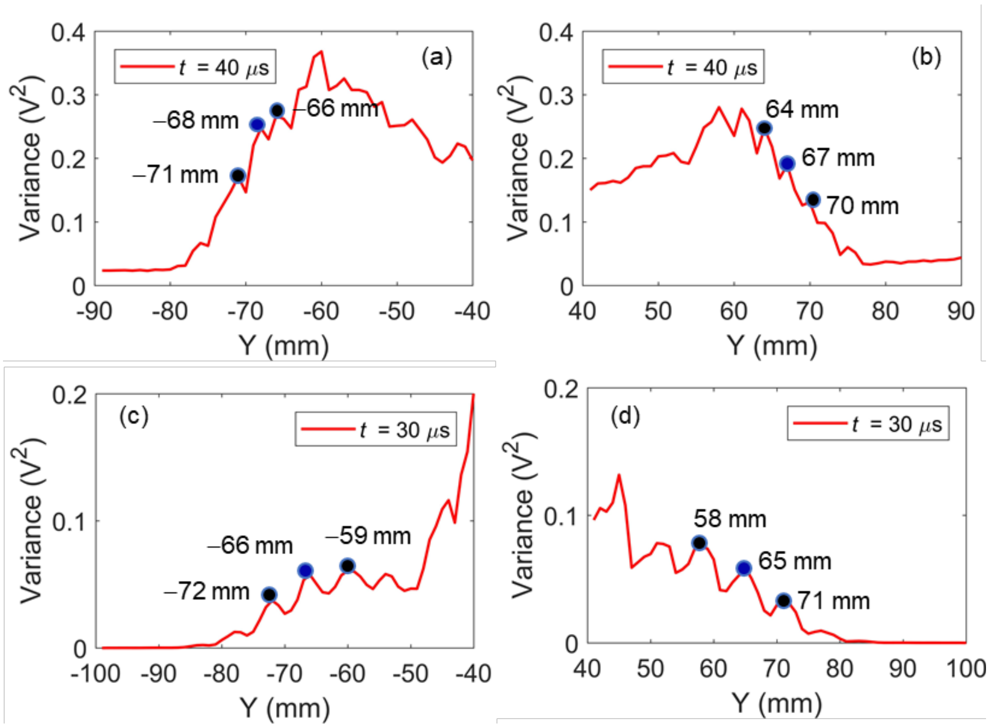

Figure 10. Zoomed view of variance signals at (a)(b) 40 μs and (c)(d) 30 μs.

Looking at the variance in the inset of Fig. 9(b), the peak responses of the S0 mode in $y < -85$ mm and $y > 85$ mm were not being able to obtain for the estimation. For that, the UWI at 30 μs was considered as shown in Fig. 9(c) and the corresponding covariance image was obtained as shown in Fig. 9(d). The inset of Fig. 9(d) shows that the multiple peaks were obtained in the ranges of –80 mm $< y <$ –50 mm and 50 mm $< y <$ 80 mm of the variance signal. Figures 10(c) and (d) show the zoomed variance signal in both ranges with the peaks locations of (–72 mm, –66 mm, and –59 mm) and (58 mm, 65 mm, and 71 mm). Both peaks locations demonstrated the ability of estimating the wavelength of the S0 mode at 13 mm and the relative error of 2.3%.

In this paper, the covariances $\mathbf{C}_X$ (Fig. 6(b)) and $\mathbf{C}_Y$(Fig. 9(b)) correspond to the spatial correlation in the x-direction and y-direction, respectively. It is observed that the variance signal (desired variance) indicates the ability to capture the wave fronts of the S0 and A0 modes when the propagation direction of these wave fronts is parallel to the spatial correlation direction. For example, the spatial correlation in the x-direction was considered in the inset of Fig. 6(b). The desired variance was obtained when the propagation direction of the wave fronts of the S0 and A0 modes was parallel to the x-direction, ranging from –60 mm to –140 mm as shown in Fig. 6(a).

In contrast, the variance signal (undesired variance) was not able to capture the wave fronts of the S0 and A0 modes when these wave fronts were not parallel to the spatial correlation direction. Since the ultrasound was emitted omnidirectionally from the Cartesian coordinate space origin as shown in Fig. 6(a), the undesired variance was obtained, ranging from 0 mm to −60 mm, when the propagation direction of the wave fronts was not parallel to the x-direction in this range. In this paper, the undesired variances are called “ripple waves” in the variance signal, which showed no relation to the wave fronts of the S0 and A0 modes. Above observations inferred that the desired variance can be only obtained when the propagation direction of the wave fronts is parallel to the considered correlation estimation direction.

Figure 3(a) shows that the propagation direction of the wave fronts in the aluminum plate was radial and symmetric in Cartesian coordinate space. Alternatively, the propagation direction of these wave fronts was also unidirectional in the R-θ plane of polar coordinate space as shown in Fig. 3(b). Subsequently, the covariance $\mathbf{C_R}$ of the R-θ plane for all k was obtained as shown in the middle of Fig. 3(b). Then, the response of $\mathbf{C_R}$ was analyzed and further verify the observations above on the emergence of the desired/undesired variance signal.

Figures 6(c) and (d) shows the wave fronts of the ultrasonic waves, ranging from −30° to 30°, propagating unidirectionally along R-axis in the R-θ plane at 40 μs and the corresponding covariance image $\mathbf{C_R}(i, j, 200)$ respectively. The covariance image showed symmetry along the diagonal and two distinguishable covariance responses in 85 mm < r < 140 mm and 50 < r < 85 mm. Similar to the Cartesian coordinate case in Figs. 6(a) and (b), the corresponding variance signal in the inset of Fig. 6(d) showed multiple peaks in the two wave packets. The first arrival distances of the wave packets were estimated at r = 140 mm and r = 85 mm which were same as the S0 and A0 modes in Fig. 6(c).

Figure 8(d) show the waveform of the ultrasound along r at $\theta = 0°$ in Fig. 6(c) with the peaks and troughs of S0 mode (120 mm, 126 mm, 133 mm) and A0 mode (66 mm, 68 mm, 71 mm). Figures 8(e) and (f) show that the peak locations of the zoomed first and second wave packets of the variance signal were same as the peak locations of the S0 and A0 mode waves in Fig. 8(d). Then, the estimated wavelengths were 13 mm and 5 mm with the deviation errors of 2.3% and 7.4% in comparison with the theoretical wavelengths of λ_1 = 13.3 mm (S0 mode) and λ_2 = 5.4 mm (A0 mode) in Fig. 2(a) at the frequency of 400 kHz, respectively.

Previously, the ripples waves were generated which were dependent upon the wave fronts' propagation direction in Cartesian coordinates. Conversely, the ripples waves of the variance signal in polar coordinate space were not generated as shown in Fig. 6(d). This was because the spatial correlation direction of the r-direction was parallel to the propagation direction of the S0 and A0 modes in the R-θ plane. Figure 8(f) shows that the peaks of A0 modes locations (r < 60 mm) were captured and able to estimate the wavelength as compared to the cases in Cartesian coordinate spaces (x > –60 mm in Fig. 8(c) and y > –60 mm in Fig. 9(b)). In addition, the peaks of variance signal in r < 60 mm have the same location to the peaks of A0 mode, for example at r = 54 mm and r = 59 mm, and the wavelength of 5 mm was estimated which was same as the estimation results obtained in previous cases.

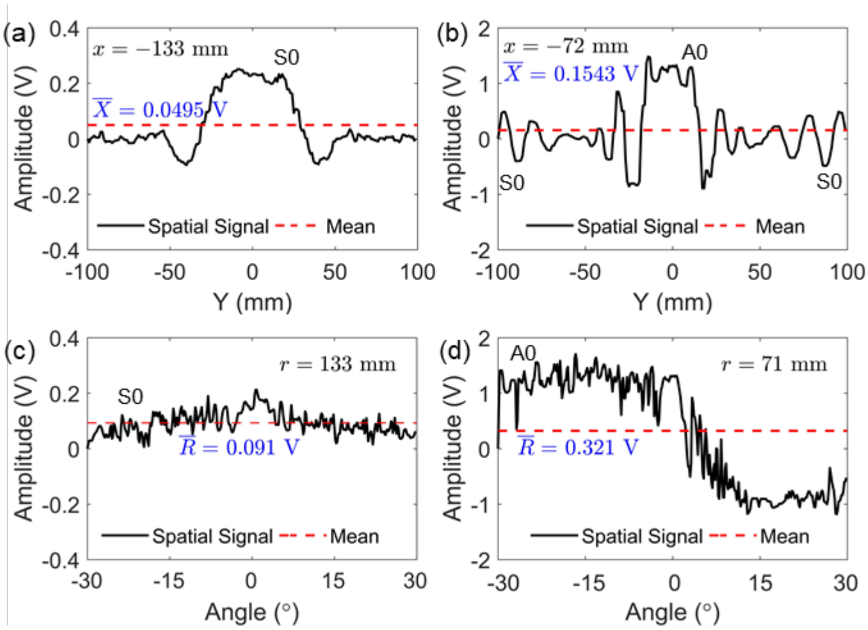

Figure 11. Spatial ultrasonic signal responses: (a) x = –133 mm and (b) –72 mm in Cartesian coordinate space, and (c) r = 133 mm and (d) 71 mm in polar coordinate space, at 40 μs respectively.

The variance signals of both coordinate spaces were different to each other as shown in the insets of Figs. 6(b) and (d). Overall, the variance signal related to S0 mode in Cartesian coordinate space was higher than the polar coordinate space, while the variance signal related to A0 mode in Cartesian coordinate space was lower than the polar coordinate space. It is because the mean values obtained in both cases were different as shown in Fig. 11.

Figures 11(a) and (b) show the spatial distances, x = –133 mm ($\mathbf{X}_{m=68}$) and x = –72 mm ($\mathbf{X}_{m=129}$) with the respective mean values of $\overline{X}_{68}$ = 0.0495 V and $\overline{X}_{129}$ = 0.1543 V for the Cartesian coordinate space. Figures 11(c) and (d) show the spatial distance, r = 133 mm ($\mathbf{R}_{p=134}$) and r = 71 mm ($\mathbf{R}_{p=72}$) with the respective mean values of $\overline{R}_{134}$ = 0.091 V and $\overline{R}_{72}$ = 0.321 V for the polar coordinate space. In previous discussion, the peaks at x = –133 mm and r = 133 mm, as related to S0 mode in Fig. 8, were the same but both mean values were different due to the difference of their variable amplitudes as shown in Figs. 11(a) and (c).

Figure 11(a) shows that the high dominant energy of S0 mode wave concentrated in between −50 mm < y < 50 mm, which led to the high variance value. Since the amplitudes of the wave fronts of the S0 mode at a given radius were same for all the circumferential angles, the amplitudes of S0 mode at r = 133 mm were about constant to the mean value for all the circumferential angles as shown in Fig. 11(c). Thus, the variances obtained in polar coordinate space were smaller than the variances obtained in Cartesian coordinate space, as shown in Figs. 8(b) and (e) which were related to S0 mode waves. Supposedly, the variance signal related to A0 mode waves is small as well since the amplitudes of the A0 mode is the same at a r with small deviation, but the variance signal of A0 mode showed high values and bigger than the variance signal in Cartesian coordinate space as shown in Figs. 8(c) and (f).

In Fig. 11(d), the amplitudes of the A0 mode at r = 71 mm in polar coordinate space were not constant, as it supposed to be constant like the S0 mode case. For that, the corresponding mean value (0.321 V) was higher than the mean value (0.1543 V) obtained in the Cartesian coordinate case and caused the high value of the variance signal in polar coordinate space. Even though the variance signal related to A0 mode was high, the corresponding peaks of the variance signal were still demonstrated in association to the wavelength of the A0 mode as discussed previously in Figs. 8(c) and (f). Authors suspected that the scan interval of 1 mm set was too high, which caused the low spatial resolution for the Cartesian-polar coordination transformation in Eqn. (4) and led to the transformation error. This transformation error may be reduced or avoided in future by using circular scanning method for LUIS instead of the raster scanning method.

4. PHASE VELOCITY ESTIMATION VIA VARIANCE MAP

In the previous section, the covariance method was employed to analyze the spatial correlation in the ultrasonic wavefield as projected in to Cartesian and polar coordinates. The method demonstrated that the variance signals have a strong relationship to the S0 and A0 modes waves when the wave fronts' propagation direction was parallel to the considered spatial correlation direction. Because of that, in the Cartesian coordinate case, the variance signal was only able to capture the wave fronts in the local spatial area, where the wave fronts propagated along x-direction or y-direction as shown in Figs. 6(a) and 9(a). In contrast, in polar coordinate case, the variance signal was able to capture all the wave fronts since they propagated unidirectionally along r-direction in R-θ plane as shown in Fig. 6(c).

Looking at these responses, the variance signal based on polar coordinates is superior as a feature for the phase and group velocities estimation compared to Cartesian coordinates. However, in this paper, the variance signal based on Cartesian coordinates was also considered as well. This is because the wave fronts in a local area of the aluminum plate have the same material properties over the aluminum plate (isotropic material), and the waves are radial and symmetric. Hence, it is still nonetheless useful to know also the feasibility of the variance signal used as a feature to estimate the phase and group velocities of the ultrasonic waves in an isotropic structure in Cartesian coordinate case.

In this paper, the variance signals related to the S0 and A0 modes, named as S0 and A0 modes variances, were formed into the variance maps ($\mathrm{var}_{\mathbf{X}}(m,k)$and $\mathrm{var}_{\mathbf{R}}(p,k)$) and were used to estimate the phase and group velocities. But, the $\mathrm{var}_{\mathbf{Y}}(n,k)$ was not considered in this paper because the S0 and A0 modes variances in the $\mathrm{var}_{\mathbf{Y}}(n,k)$ (Fig. 5(b)) were not separated sufficiently in time, especially for the S0 and A0 modes with the larger wavelength, for the phase and group velocities estimation.

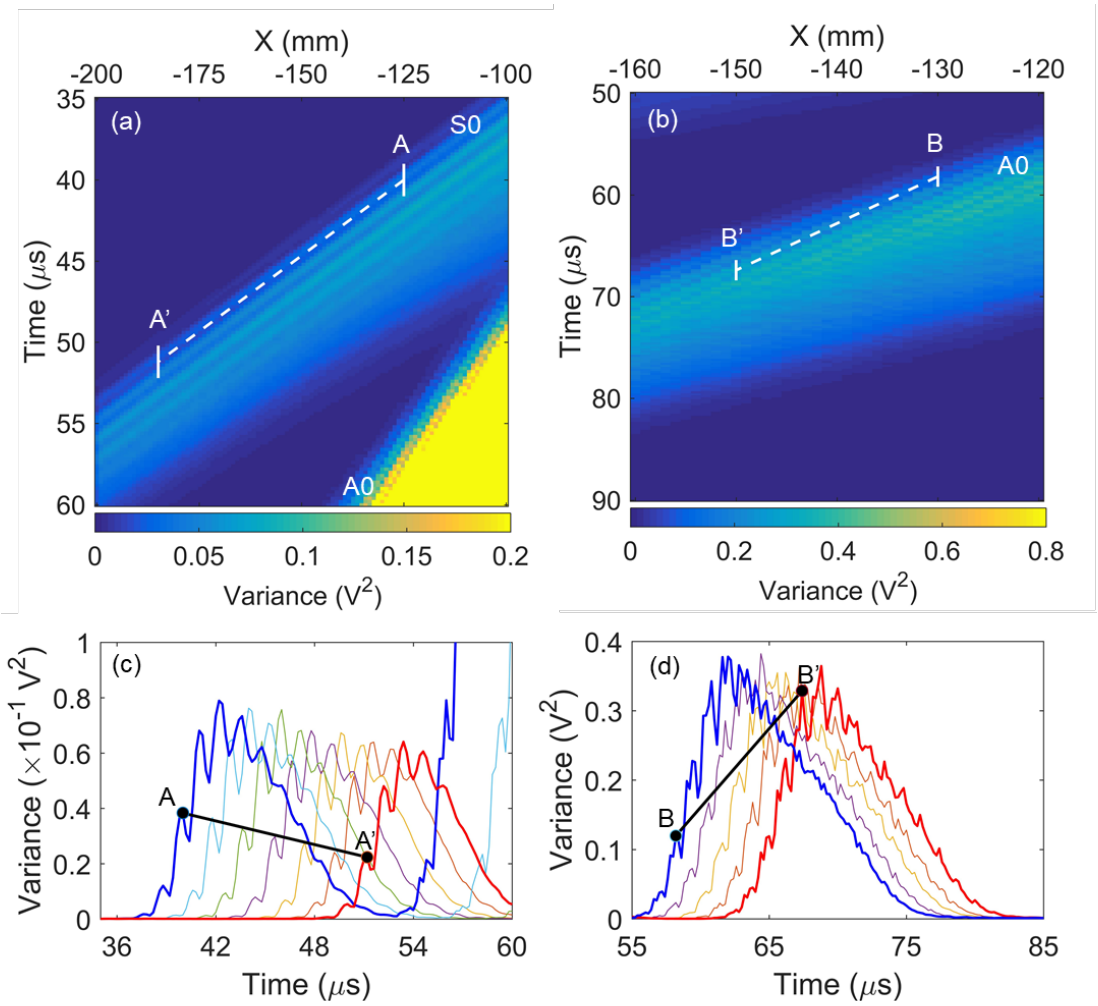

Figure 12. Cartesian coordinate space: Zoomed views of variance map (a) S0 mode and (b) A0 mode and arbitrary variance signals between (c) AA′ and (d) BB′.

First, the change of S0 and A0 modes variances in time domain in the $\text{var}_{\mathbf{X}}(m,k)$ and $\text{var}_{\mathbf{R}}(p,k)$ were investigated in order to be used for the phase and group velocities estimation.

Figures 12(a) and (b) show the zoomed view of the S0 mode and A0 mode variances in the $\text{var}_{\mathbf{X}}(m,k)$ in Fig. 5(a) respectively. The ridges and grooves were observed in both zoomed variance maps. As explained in previous section, the variance map was formed by mapping each variance signal of covariance matrix, hence these ridges and grooves in the variance map were formed by the peaks and troughs of the S0 and A0 modes variances for all time-index *k*. Regards to this, a ridge in the variance map was representing a peak of S0 or A0 mode variance propagation along a spatial distance as time evolved.

Figures 12(a) and (b) show the shaded white lines from point A(–126 mm, 40 μs) to point A′(–186 mm, 51.2 μs) and from point B (–131 mm, 58.2 μs) to point B′(–151 mm, 67.4 μs) along the same ridges of S0 and A0 modes variances, respectively. Figure 12(c) shows a series of the corresponding S0 mode variances in Fig. 12(a), ranging from −126 mm to −186 mm. The variance peak was propagated from the point A(–126 mm) to the point A′(–186 mm) and the corresponding variance value was reduced as the time increased from 40 μs to 51.2 μs. Figure 12(d) shows a series of the corresponding A0 mode variances in Fig. 12(b) ranging from –131 mm to –151 mm. The variance peak was propagated from the point B to B′ but the corresponding variance value was increased which was differed from the S0 mode variances.

A series of the 1-D spatial ultrasonic signals along spatial samples *x* at *y* = 0 mm in the UWI as shown in Fig. 6(a) was extracted from 40 μs to 51.2 μs and 58.2 μs to 67.4 μs to investigate the amplitude response of the S0 and A0 modes variances as time evolved.

Figure 13(a) shows the extracted 1-D spatial ultrasonic signals from 40 μs to 51.2 μs. The location of the blue solid circle (the top of Fig. 13(a)) at the trough (–126 mm) of the S0 mode wave was same to the location and time of the peak at A in Fig. 12(c). As the time progressing, the blue solid circle indicated that the same trough of the S0 mode propagated to the point (the bottom of Fig. 13(a)) that has the same location of the peak A′ of the variance signal in Fig. 12(c).

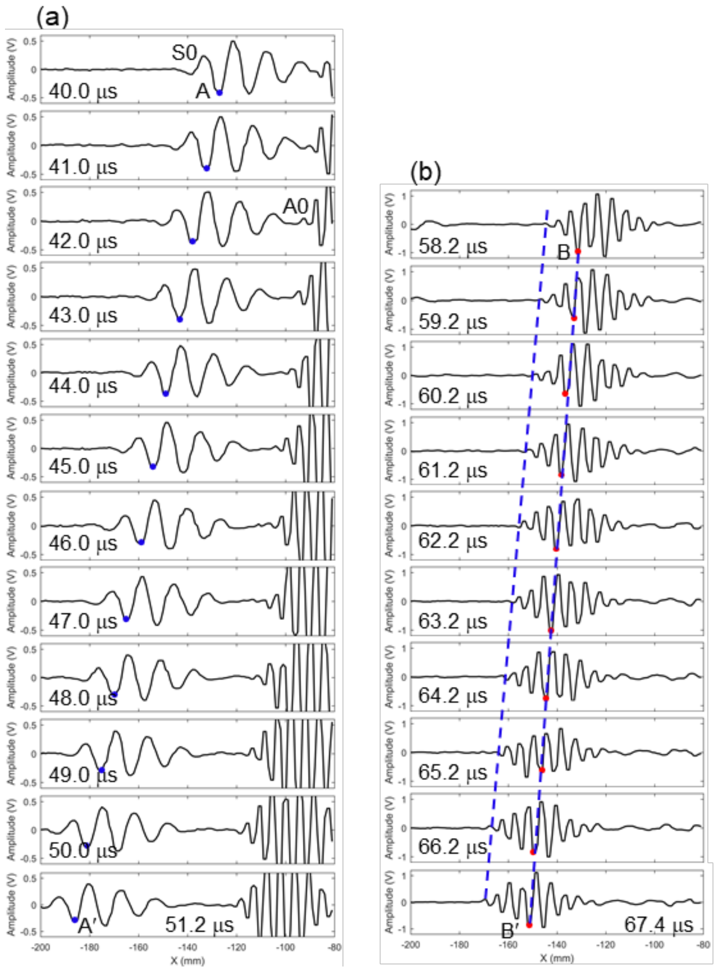

Figure 13. Cartesian coordinate space: Corresponding Lamb waves (a) S0 mode and (b) A0 mode between points AA′ and BB′ respectively.

For A0 mode waves at 58.2 µs, the red solid circle (the top of the Fig. 13(b)) located at the trough (−131 mm) was also same to the location and time of the peak at B in Fig. 12(d). The red solid circle indicates also that the same trough of the A0 mode propagated linearly to the point (the bottom of Fig. 13(b)) that same to the peak B′ of the variance signal in Fig. 12(d). These demonstrated that the peaks of the variance signals in Figs. 12(c) and (d) for all *k* were related to the S0 and A0 modes as time evolved. This was demonstrated that the earlier claimed of the two peaks at the different points along the same ridges were the same as time evolved.

For that, the phase velocity of the S0 and A0 modes may be determined in the variance map in space-time domain based on the following expression:

$$V_p = \left|\left(d_2 - d_1\right)\right| / \left(t_2 - t_1\right) \tag{6}$$

where, d_1 and d_2 are the selected two spatial points on the same ridge along the spatial sample of the variance map, and t_1 and t_2 are the corresponding times. For example, the phase velocity of S0 mode at 400 kHz from the two points A(d_1 = −126 mm, t_1 = 40 μs) and A′(d_1 = −186 mm, t_2 = 51.2 μs) was determined at 5357.1 m/s with the relative errors of 0.2% to the theoretical phase velocity of 5344.5 m/s (Fig. 2(a)). Then, the phase velocity of the A0 mode at 400 kHz was determined at 2173.9 m/s with the relative errors of 0.38% to the theoretical phase velocity of 2182.24 m/s.

For the A0 mode wave at 400 kHz, the theoretical phase velocity (2182.24 m/s) is slower than the group velocity (3077.88 m/s) and the phenomena was demonstrated in Fig. 13(b). The location of the red solid circle (B) was 2.5λ (λ denoted as one wavelength of the A0 mode wave) away from the first arrival wave (shaded blue line) of the A0 mode wave at 58.2 μs as shown in the top of Fig. 13(b). Then, when the time was at 67.4 μs, the location of the red solid circle (B′) was moved 3.5λ away from the first arrival wave of the A0 mode wave as shown in the bottom of Fig. 13(b). The increment of the number of the wavelength demonstrated that the group velocity was faster than the phase velocity which was showed good agreement to the theoretical phase and group velocities curves in Fig. 2. Figure 13(b) shows also that the amplitude of the peak corresponding to the red solid circle was increased due to the increment of group energy as the wave packet propagating from 58.2 μs to 67.4 μs as shown in Fig. 12(d). With that, the variance values are associated with the energy of the S0 and A0 modes as they travel, which is an interesting topic for future consideration.

For polar coordinate space, Figs. 14(a) and (b) show the zoomed view of the S0 mode and A0 mode variances in the $\mathrm{var}_{\mathbf{R}}(p,k)$ in Fig. 5(c) respectively. Figures 14(a) and (b) show the shaded white lines from point C(75 mm, 30 μs) to point C′(125 mm, 39.4 μs) and from point D(75 mm, 39 us), point D′(95 mm, 48.2 us) to point D″(125 mm, 61.8 us) along the same ridges, respectively. Similar to Cartesian coordinate case, the peak travelling from C to C′ was the same, as well as the peak from D, D′ to D″.

Figure 14(c) shows a series of the corresponding S0 mode variances in Fig. 14(a) ranging from 75 mm to 125 mm. The S0 mode variance peak was propagated from C to C′ as the time evolved from 30 μs to 39.4 μs. In the same manner, by comparing to the 1-D signals of S0 mode waves in Fig. 15(a), the amplitude (blue solid circle) of the trough of the S0 mode wave demonstrated related to the S0 mode variance peak from 30 μs to 39.4 μs in Fig. 14(c).

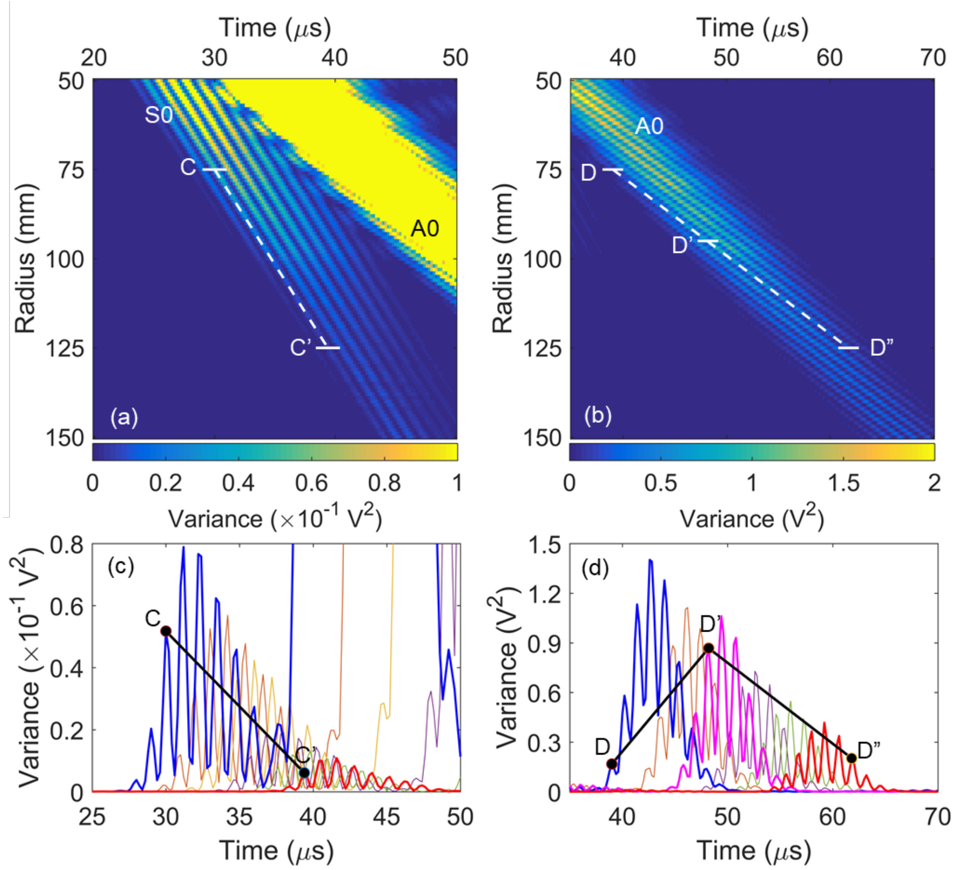

Figure 14. Polar coordinate space: Zoomed views of variance map (a) S0 mode and (b) A0 mode and arbitrary variance signals between (c) CC′ and (d) DD″.

Figure 14(d) shows a series of the corresponding A0 mode variances in Fig. 14(b), ranging from 75 mm to 125 mm. Figure 14(d) shows that the variance peak value was raised from D to D′ and then declined back from D′ to D″. In previous case, as shown in Fig. 13(b), the variance values were related to the amplitudes of the A0 mode wave and changed due to the difference of the group velocity and phase velocity. Hence, as shown in Fig. 15(b), the wavelength difference between first arrival wave of the A0 mode wave packet and the red solid circle (the same location of D in Fig. 14(d)) was 0.5λ and then this wavelength difference was increased to 4.5λ from 39 μs to 61.8 μs as the red solid circle travelling to 125 mm (D″). During this wave propagation, the amplitude at the red solid circle (Fig. 15(b)) was increased negatively from –0.3987 V (at 75 mm and 39 μs) to –1.0740 V (at 95 mm and 48.2 μs) and then decreased negatively back to –0.5864 V (at 125 mm and 61.8 μs). The change of the amplitude at these three different space-time points was caused to the change of the variance value at D, D′ and D″.

Based on Eqn. (6), the phase velocity of S0 mode at 400 kHz from the two points C(d_1 = 75 mm, t_1 = 30 μs) and C(d_2 = 125 mm, t_2 = 39.4 μs) was determined at 5319.1 m/s with the relative errors of 0.5% to the theoretical phase velocity of 5344.5 m/s (Fig. 2(a)). For A0 mode, the phase velocities were determined at 2173.9 m/s (D(d_1 = 75 mm, t_1 = 39 μs) to D′(d_2 = 95 mm, t_2 = 48.2 μs)) and 2205.9 m/s (D′(d_1 = 95 mm, t_1 = 48.2 μs) to D″(d_1 = 125 mm, t_1 = 61.8 μs)) with the relative errors of 0.38% and 1.08% in comparison to the theoretical phase velocity of 2182.24 m/s.

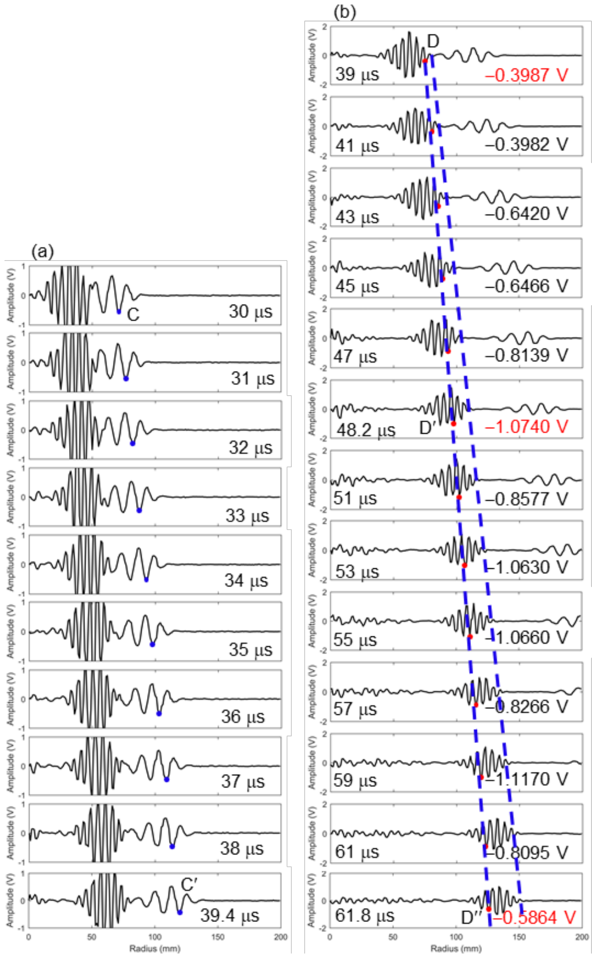

Figure 15. Polar coordinate space: Corresponding Lamb waves (a) S0 mode and (b) A0 mode between points CC′ and DD″ respectively.

Based on the previous analysis in Figs. 12 and 14, the variance map was demonstrated that the map may be used as an alternative method for the phase velocities estimation of S0 and A0 modes. In this paper, ten variance maps of $\mathbf{C_X}$ generated for each five different frequencies were obtained and the ten measurements of the corresponding phase velocities for each frequency points were measured based on Eqn. (6). As shown in Fig. 16, the measured phase velocities of S0 and A0 modes based on $\mathbf{C_X}$ and $\mathbf{C_R}$, denoted as V_P^{S0} and V_P^{A0}, were plotted to compare with the theoretical phase velocities curves as plotted in solid lines. The mean phase velocities of S0 and A0 modes, denoted as $\overline{V}_P^{S0}$ and $\overline{V}_P^{A0}$, were calculated as well and plotted in Fig. 16. Figure 16 shows that the measured and mean phase velocities demonstrated good agreement to the theoretical phase velocity curves in both coordinate spaces.

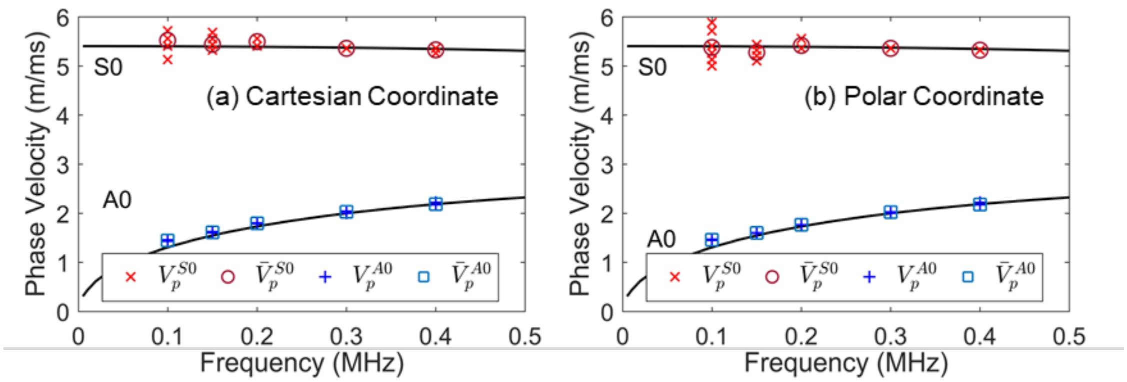

Figure 16. Theoretical phase velocity curves and phase velocity measurements for S0 and A0 modes in (a) Cartesian coordinate and (b) polar coordinate spaces.

Tables 1 and 2 present the mean phase velocity and the corresponding mean relative errors for both coordinate spaces. Table 1 shows that the S0 mode phase velocities at 100 kHz were measured with the mean velocities of 5561.57 m/s and 5357.42 m/s and standard deviations of ±192.97 m/s and ±248.26 m/s for both coordinate spaces respectively. Then, both corresponding mean relative errors were the highest deviations with 3.51% and 3.76% as compared to the other measurements as shown in Table 2. On the other hand, the S0 mode phase velocities at 300 kHz were precisely measured with the mean velocity of 5357.14 m/s and zero standard deviation for both coordinate spaces. Furthermore, the S0 mode phase velocities at 300 kHz were accurately measured with the lowest mean relative errors of 0.29% among the measurements as shown in Table 2.

For A0 mode, the phase velocities at 100 kHz were measured with the mean velocities of 1393.83 m/s and 1460.94 m/s and the measurements were less accurate with the highest relative errors of 5.91% and 11.00% (Table 2) as compared to the other measurements for Cartesian and polar coordinate spaces respectively. In contrast, the phase velocities of A0 mode at 400 kHz were measured with high accuracy at the relative errors of 0.62% and 0.48% for both coordinate spaces as shown in Table 2.

Table 2 shows also the tendency of the accuracy for both S0 and A0 modes phase velocities was to reduce as the frequency decreases. The highest mean relative errors in the phase velocities of A0 mode at 100 kHz were obtained might due to the high dispersive characteristic for A0 mode waves at the low frequency ranges, where the dispersion might be caused by the specimen surface quality. Besides that, the high errors in the estimation is also because the bandwidth set in the bandpass filter during the signal acquisition in the in-line filter since the bandwidth of the filter has the influence in the phase velocity estimation [18]. The mean relative errors of S0 mode waves at 100 kHz were the highest among the measurements. This was suspected that the S0 and A0 modes was not separated sufficiently in time since the long wavelength of the S0 mode waves was generated at 100 kHz.

Table 1. Mean phase velocity measurements of S0 and A0 modes.

Phase Velocity (m/s)		Frequency (kHz)				
		100	**150**	**200**	**300**	**400**
		Cartesian Coordinate Space				
S0	**Mean ($\bar{V}_P^{S0}$)**	5561.57	5436.87	5495.50	5357.14	5328.95
	Standard Deviation	192.97	113.37	77.54	0	45.40
A0	**Mean ($\bar{V}_P^{A0}$)**	1393.83	1610.86	1795.37	2028.57	2183.57
	Standard Deviation	12.33	8.20	8.31	19.72	20.37
		Polar Coordinate Space				
S0	**Mean ($\bar{V}_P^{S0}$)**	5357.42	5275.76	5416.67	5357.14	5319.15
	Standard Deviation	248.26	93.40	95.84	0	0
A0	**Mean ($\bar{V}_P^{A0}$)**	1460.94	1600.52	1764.71	2024.32	2178.74
	Standard Deviation	46.24	4.30	0	8.55	15.28

Table 2. Mean relative errors of mean phase velocity of S0 and A0 modes.

Relative Error of Phase Velocity (%)		Frequency (kHz)				
		100	**150**	**200**	**300**	**400**
		Cartesian Coordinate Space				
S0	**Mean**	3.51	1.62	1.96	0.29	0.62
	Standard Deviation	3.02	1.47	1.44	0	0.62
A0	**Mean**	5.91	4.00	3.92	1.42	0.67
	Standard Deviation	0.09	0.53	0.48	0.96	0.61
		Polar Coordinate Space				
S0	**Mean**	3.76	2.36	1.35	0.29	0.48
	Standard Deviation	2.48	1.5	1.2	0	0
A0	**Mean**	11.00	3.34	2.14	1.19	0.53
	Standard Deviation	0.46	0.28	0	0.41	0.46

5. GROUP VELOCITY ESTIMATION VIA VARIANCE MAP

In previous section, the variance signal demonstrated related to the Lamb waves S0 and A0 modes in UWI and the ability to estimate the phase velocities of the S0 and A0 modes. Now, the variance map is further used to estimate the group velocities of the S0 and A0 modes waves in Cartesian coordinate and polar coordinate spaces.

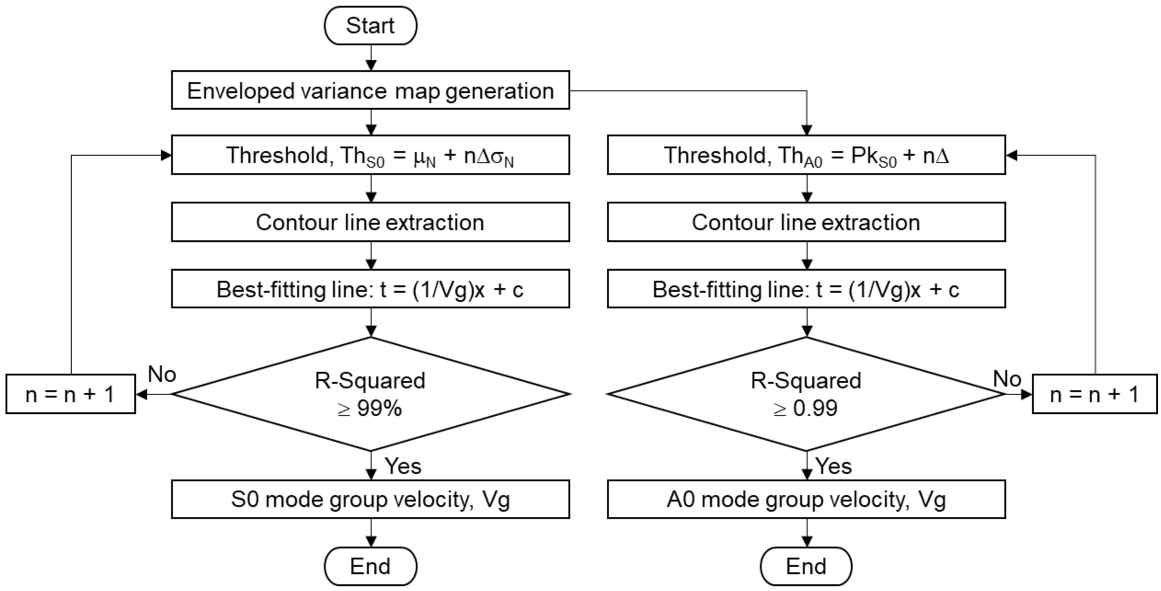

Figure 17. Flow chart of S0 and A0 modes group velocity estimation algorithm.

Figure 17 shows the flow chart of S0 and A0 modes group velocities estimation algorithm. First, the variance signals in the variance map are enveloped. As shown in Fig. 18, to obtain enveloped variance map, all variance signals in time-domain are enveloped for all spatial samples using the peak envelope function, "*envelope*", from MATLAB R2017b. In the envelope process, the peaks of the variance signal are extracted and then interpolated by the spline interpolation algorithm to obtain the envelope of the signal. For example, a variance signal at $x = -150$ mm (Fig. 18) was extracted from the variance map, the corresponding peaks were extracted (blue dots), and the corresponding peaks were interpolated (red curve). Then, the enveloped variance map is generated by repeating the same envelope process to the variance signal for all the spatial samples and mapping all the enveloped variance signals into 2D array matrix form as shown in the left bottom of Fig. 18.

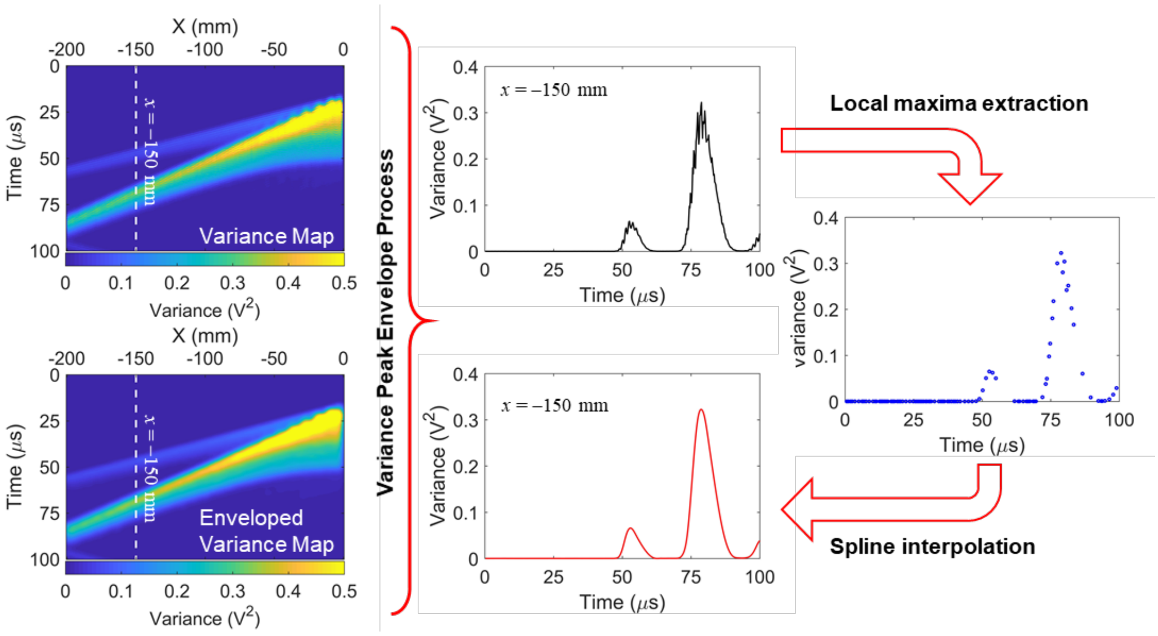

Figure 18. Schematic diagram of enveloped variance map process based on peak envelope method using spline interpolation over local maxima method (MATLAB, R2017b).

The enveloped variance map is then plotted in the contour format as shown in Fig. 19(a). Figure 19(a) shows that the variance waves of the modes are visualized as multiple contour lines. Since the wave fronts of S0 and A0 modes waves are related to variance waves, the first arrival wave fronts of the variance waves may be determined by extracting the contour line based on the threshold-crossing method. In this paper, as shown in Fig. 19(a), the wave fronts of the variance wave related to S0 mode wave were distinguishable and represented as a contour line. Hence, to extract the first arrival of the variance wave related to S0 mode wave, the threshold crossing method is employed and the threshold level is set based as

$$Th_{S0} = \mu_N + n\Delta\sigma_N \tag{7}$$

where n is iteration integer number (0, 1, 2, …), Δ is increment (step), and σ_N is the standard deviation of the variance noise (Fig. 19(a)). The mean noise μ_N is determined by averaging all the variance noise at time 0 μs for all spatial x samples as shown in Fig. 19(a).

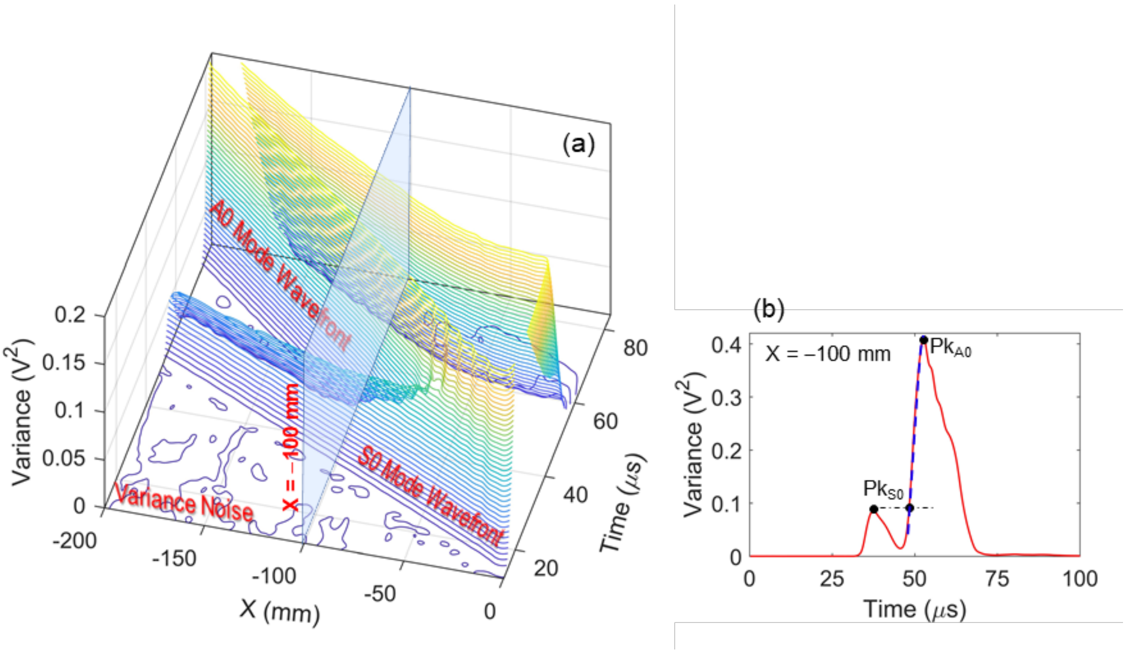

Figure 19. (a) Contour plot of enveloped variance map and (b) enveloped variance signal at X = −100 mm.

On the other hand, for A0 mode, the first arrival of the variance wave related to A0 mode wave is complex to estimate based on Eqn. (7) because the wave front of the variance wave might interfere with the residual waves of the S0 mode. Commonly, the signal-to-noise ratio (SNR) of S0 mode waves is weaker than the SNR of A0 mode as shown in Fig. 19(b). Thus, the peak of the S0 mode variance wave packet (Pk_{S0}) is assigned as an initial value of the threshold level, and the threshold level is expressed as below:

$$Th_{A0} = Pk_{S0} + n\Delta \tag{8}$$

where, n is iteration integer number (0, 1, 2, …), Δ is increment (step), and Th_{A0} is set only valid in the range of from Pk_{S0} to Pk_{A0}(the peak of A0 mode wave packet as shown in Fig. 19(b)).

The Pk_{S0} is selected by opting the second highest peak in the enveloped variance signal with the consideration of no enveloped variance signals that related to the reflected waves in the enveloped variance signal since in some cases the reflected waves may be higher than the Pk_{S0}. Hence, the enveloped variance signal related to the reflected signal is singled out before the peak selection process by setting the prior known time range from the variance map. For example, the variance map based on the frequency of 400 kHz was set with the time range of from 0 µs to 100 µs as shown in Figs. 5(a) and (c). On the other frequency case, the time range was changed to larger time range since the A0 mode wave at lower frequency needs a longer time to propagate as due to its lower group velocity. Thus, in this paper, the larger time range of from 0 μs to 250 μs was set for the proposed frequency of 100 kHz as shown in Fig. 20(a), and this time range was also set for the proposed frequency of 150 kHz.

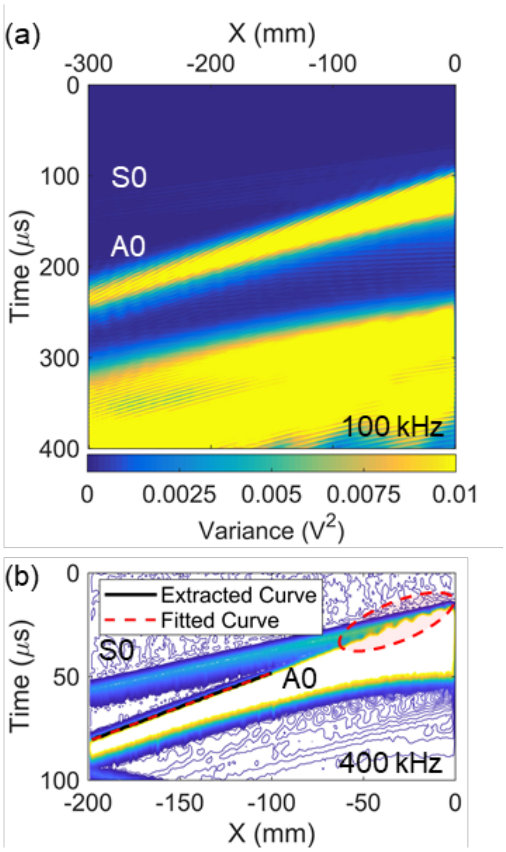

Figure 20. Enveloped variance maps at (a) 100 kHz and (b) 400 kHz.

Given that the contour line is associated with the Lamb wave fronts as shown in Fig. 19(a), the linearity of that contour line may then be used to estimate the group velocity via linear regression fit. However, the contour line is not perfectly straight, especially for the wave fronts generated in the near-field, e.g., the shaded circle as shown in Fig. 20(b). Subsequently, to avoid obtaining inaccurate estimation, the starting point of the contour line is considered at a point that is far away from the sensor. In this paper, the distance range was set from −50 mm to −150 mm for the S0 mode group velocity estimation for the proposed frequencies. As for the A0 mode group velocity estimation, the distance range for the proposed frequencies of 200, 300, and 400 kHz was set from −100 mm to −150 mm, and then distance range for the proposed frequencies of 100 and 150 kHz was set to −150 mm to −200 mm.

After the threshold level and the two spatial endpoints of the contour line are set, the extraction process (Fig. 17) starts to extract the contour line based on the threshold level set. When the corresponding contour line is crossed the present threshold level, the contour line is then linearly regressed as shown in the flow chart in Fig. 17. If the fitted model is obtained with R-squared more than or equal to a preset R-squared, then the corresponding gradient ($1/V_g$) of the linear model is extracted, else a new threshold level in Eqn. (7) or (8) will be set by increasing the n to extract another new contour line for the next fitting process to estimate the group velocity of the S0 mode or the A0 modes. Lastly, the group velocities of S0 mode or A0 mode are determined by inverting the gradient of the linear model. In this paper, the Δ in Eqns.(7) and (8) was arbitrarily set to 0.001 and R-squared was set to 99% for both modes group velocities estimation process. The estimation process discussed above was repeated to estimate the group velocity for all the frequencies that were set to develop the group velocity curves for S0 and A0 modes.

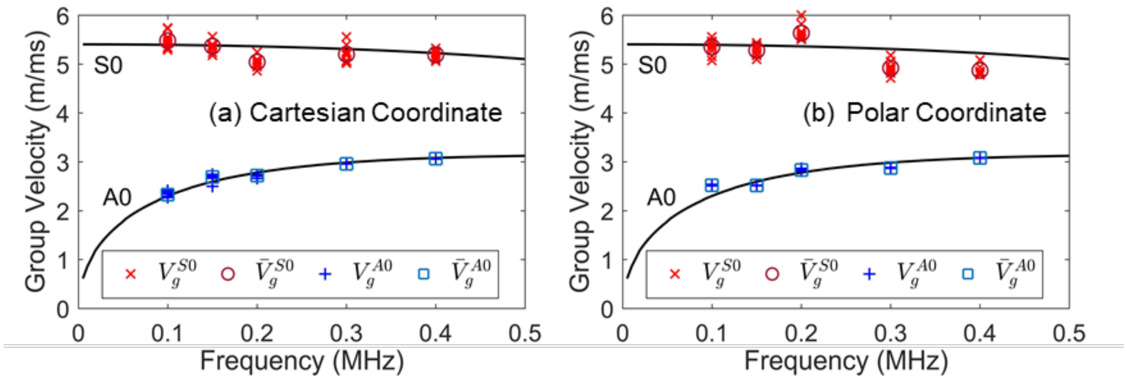

Figure 21. Theoretical group velocity curves and group velocity measurements for S0 and A0 modes in (a) Cartesian coordinate and (b) polar coordinate spaces.

Figures 21(a) and (b) show the measured group velocities of the S0 and A0 modes for Cartesian and polar coordinate spaces, denoted as V_g^{S0} and V_g^{A0}, respectively. The mean group velocities, denoted as $\bar{V}_g^{S0}$ and $\bar{V}_g^{A0}$, were calculated as well and plotted in Fig. 21. The measured and mean group velocities indicated good agreement with the theoretical group velocities for both S0 and A0 modes.

Tables 3 and 4 present the mean group velocity and the corresponding mean relative errors for both coordinate spaces. Table 3 shows that the group velocities of S0 and A0 modes for both coordinate spaces were less precise as compared to the measurement of the phase velocity in Table 1.

In Cartesian coordinate space, the group velocities of S0 mode at 300 kHz were measured at the mean group velocity of 5199.18 m/s and less precise as compared to other measurements with the highest standard deviation of 175.53 m/s. But, the measured group velocity of the S0 mode at 300 kHz was more accurate as compared to the measurement at 200 kHz that was the highest mean relative errors of 5.97%. As for in polar coordinate space, the group velocities of S0 mode at 200, 300, and 400 kHz were measured less accurate as compared to the Cartesian coordinate space and the corresponding mean relative errors were 5.06%, 7.31%, and 6.80% respectively. In both coordinate spaces, the group velocities of S0 mode were measured with high mean relative errors as the frequencies increased and this might due to the wave packet of the S0 mode was getting dispersive as the frequency increased.

Figure 21 shows that the A0 group velocity measurement was more accurate than the S0 mode group velocity. This was because that the S0 mode has low SNR and may easily get contaminated by the noise as compared to the A0 mode. In polar coordinate space, the group velocity of the A0 mode at 100 kHz has the highest mean relative errors at 10.55% and it might due to the A0 mode wave at this frequency was highly dispersive as compared to the other. Table 4 shows also that the group velocities at the frequency of 400 kHz for both coordinate spaces were measured accurately with only mean relative error, as low as 0.09%.

Table 3. Mean group velocity measurements of S0 and A0 modes.

Group Velocity (m/s)		**Frequency (kHz)**				
		100	**150**	**200**	**300**	**400**
		Cartesian Coordinate Space				
S0	**Mean ($\overline{V}_g^{S0}$)**	5478.55	5366.55	5042.54	5199.18	5188.04
	Standard Deviation	158.07	122.57	102.27	175.53	84.24
A0	**Mean ($\overline{V}_g^{A0}$)**	2327.91	2721.81	2717.48	2958.17	3062.64
	Standard Deviation	52.62	24.59	22.44	2.82	3.50
		Polar Coordinate Space				
S0	**Mean ($\overline{V}_g^{S0}$)**	5350.15	5281.60	5633.82	4919.16	4869.48
	Standard Deviation	148.80	103.37	161.25	127.33	93.57
A0	**Mean ($\overline{V}_g^{A0}$)**	2519.08	2514.96	2831.53	2872.53	3077.97
	Standard Deviation	8.83	1.87	19.69	5.33	4.09

Table 4. Mean relative errors of mean group velocity of S0 and A0 modes.

Relative Error of Group Velocity (%)		**Frequency (kHz)**				
		100	**150**	**200**	**300**	**400**
		Cartesian Coordinate Space				
S0	**Mean**	2.46	1.69	5.97	3.29	1.38
	Standard Deviation	2.16	1.45	1.91	1.87	1.02
A0	**Mean**	2.27	4.85	2.10	0.68	0.50
	Standard Deviation	2.19	0.95	0.81	0.09	0.11
		Polar Coordinate Space				
S0	**Mean**	2.09	2.05	5.06	7.31	6.80
	Standard Deviation	1.85	1.66	3.00	2.40	1.79
A0	**Mean**	10.55	3.12	2.01	3.55	0.09
	Standard Deviation	0.39	0.07	0.71	0.18	0.09

6. CONCLUSION

In this paper, a spatial covariance matrix was employed to statistically investigate ultrasonic wavefield imaging based on laser ultrasonic generation on a 2-mm aluminum plate. The covariance matrix was generated and formed in covariance imaging based on the vector variables of $\mathbf{X}_m$ and $\mathbf{Y}_n$ in Cartesian coordinate space and $\mathbf{R}_p$ in polar coordinate space for all time samples. The relationships between the UWI and the convariance imaging were analyzed and the findings are summarized as follows:

- A variance (covariance diagonals) signal showed a strong relationship to the S0 and A0 modes waves when the wave fronts of the S0 and A0 modes propagate parallel to an axis which is taken for the covariance matrix calculation.
- The circumferential ultrasound demonstrated the variance signal obtained more accurate by generating all the peaks in relation to all the wave fronts of the S0 and A0 modes.
- The peaks of the variance signal in space domain in variance map demonstrated a relation to the wave fronts of S0 and A0 modes and these peaks were able to estimate the wavelength of the S0 and A0 modes.
- The peaks of the variance signal in the time domain in variance map demonstrated relation to the wave propagation of S0 and A0 modes and these peaks were able to estimate the phase and group velocities of the S0 and A0 modes.

Based on these findings, the variance maps and enveloped variance maps for both coordinate spaces were generated to estimate the phase velocities and group velocities of the S0 and A0 modes respectively at five different frequencies to develop the dispersion curves. The estimated dispersion curves showed good agreement to the theoretical dispersion curves. These promising results made the variance map a new alternative approach for phase and group velocities dispersion curve estimation, often needed for ultrasonic NDE/SHM applications.

In this study, it was also found that the settings of the scanning area and the scanning interval depend upon the considered frequency region of the dispersion curves. When a lower frequency region is considered, the scanning area may need to set large enough for the longer wavelength of the mode to be fully spatially observable. Of course, the wavelength of the mode decreases as the frequency increases. In general, the scanning area must be set in accordance with the given mode's spatial Nyquist theorem. Thus, given an appropriate scanning interval, the proposed method may be used to estimate the velocity of arbitrarily higher modes (S1, A1, etc.). Moreover, the ultrasound generated by the pulsed laser is normally in the broadband frequency range, up to few megahertz, where the higher modes appear.

Since the covariance matrix demonstrated the ability to extract the features of S0 and A0 modes, a new development of damage detection algorithms based on the variance-covariance matrix may be possible. Future will consider more complex, anisotropic (e.g., composite) structures for dispersion curve estimation via the variance map based on polar coordinate space.

Acknowledgement

The authors acknowledge funding from UC Office of the President for partial support of this work.

References

[1] J.-B. Ihn and F.-K. Chang, "Detection and monitoring of hidden fatigue crack growth using a built-in piezoelectric sensor/actuator network: I. Diagnostics," *Smart Materials and Structures,* vol. 13, p. 609, 2004.

[2] S. C. Rosalie, M. Vaughan, A. Bremner, and W. K. Chiu, "Variation in the group velocity of Lamb waves as a tool for the detection of delamination in GLARE aluminum plate-like structures," *Composite Structures,* vol. 66, pp. 77-86, 10// 2004.

[3] F. Ciampa and M. Meo, "A new algorithm for acoustic emission localization and flexural group velocity determination in anisotropic structures," *Composites Part A: Applied Science and Manufacturing,* vol. 41, pp. 1777-1786, 12// 2010.

[4] M. Ruzzene, "Frequency–wavenumber domain filtering for improved damage visualization," *Smart Materials and Structures,* vol. 16, p. 2116, 2007.

[5] E. B. Flynn, S. Y. Chong, G. J. Jarmer, and J.-R. Lee, "Structural imaging through local wavenumber estimation of guided waves," *Ndt & E International,* vol. 59, pp. 1-10, 2013.

[6] S. M. Ziola and M. R. Gorman, "Source location in thin plates using cross-correlation," *The Journal of the Acoustical Society of America,* vol. 90, pp. 2551-2556, 1991.

[7] A. H. Kocaoglu and L. T. Long, "A Review of Time-Frequency Analysis Techniques for Estimation of Group Velocities," *Seismological Research Letters,* vol. 64, pp. 157-167, 1993.

[8] R. Raya, A. Frizera, R. Ceres, L. Calderón, and E. Rocon, "Design and evaluation of a fast model-based algorithm for ultrasonic range measurements," *Sensors and Actuators A: Physical,* vol. 148, pp. 335-341, 2008/11/04/ 2008.

[9] B. Xu, L. Yu, and V. Giurgiutiu, "Advanced methods for time-of-flight estimation with application to Lamb wave structural health monitoring," in *7th International Workshop on Structural Health Monitoring*, Stanford University, 2009.

[10] J.-R. Lee, S. Y. Chong, H. Jeong, and C.-W. Kong, "A time-of-flight mapping method for laser ultrasound guided in a pipe and its application to wall thinning visualization," *NDT & E International,* vol. 44, pp. 680-691, 12// 2011.

[11] S. Y. Chong, J.-R. Lee, and Y. P. Chan, "Statistical threshold determination method through noise map generation for two dimensional amplitude and time-of-flight mapping of guided waves," *Journal of Sound and Vibration,* vol. 332, pp. 1252-1264, 3/4/ 2013.

[12] P. White, "Cross correlation in structural systems: dispersion and nondispersion waves," *The Journal of the Acoustical Society of America,* vol. 45, pp. 1118-1128, 1969.

[13] W. Prosser, M. D. Seale, and B. T. Smith, "Time-frequency analysis of the dispersion of Lamb modes," *The Journal of the Acoustical Society of America,* vol. 105, pp. 2669-2676, 1999.

[14] H. Jeong and Y.-S. Jang, "Wavelet analysis of plate wave propagation in composite laminates," *Composite Structures,* vol. 49, pp. 443-450, 2000/08/01/ 2000.

[15] M. Niethammer, L. J. Jacobs, J. Qu, and J. Jarzynski, "Time-frequency representations of Lamb waves," *The Journal of the Acoustical Society of America,* vol. 109, pp. 1841-1847, 2001.

[16] P. Alessandro, M. Luca De, M. Alessandro, and S. Nicolò, "Acoustic emission localization in plates with dispersion and reverberations using sparse PZT sensors in passive mode," *Smart Materials and Structures,* vol. 21, p. 025010, 2012.

[17] B. Xu, V. Giurgiutiu, and L. Yu, "Lamb waves decomposition and mode identification using matching pursuit method," in *SPIE Smart Structures and Materials + Nondestructive Evaluation and Health Monitoring*, 2009, p. 12.

[18] L. Draudvilienė and L. Mažeika, "Measurement of the group velocity of Lamb waves in aluminum plate using spectrum decomposition technique," *Ultragarsas" Ultrasound",* vol. 66, pp. 34-38, 2011.

[19] L. Draudvilienė and L. Mažeika, "Investigation of the spectrum decomposition technique for estimation of the group velocity Lamb waves," *Ultragarsas" Ultrasound",* vol. 66, pp. 13-16, 2009.

[20] J. S. Hall and J. E. Michaels, "A model-based approach to dispersion and parameter estimation for ultrasonic guided waves," *The Journal of the Acoustical Society of America,* vol. 127, pp. 920-930, 2010.

[21] G. J. Jarmer, E. B. Flynn, and M. D. Todd, "Dispersion curve estimation via phased array beamforming methods," *Journal of Intelligent Material Systems and Structures,* vol. 25, pp. 563-574, 2014.

[22] L. Draudvilienė and L. Mažeika, "Analysis of the zero-crossing technique in relation to measurements of phase velocities of the S0 mode of Lamb waves," *Ultragarsas" Ultrasound",* vol. 65, pp. 11-14, 2010.

[23] L. Mažeika and L. Draudvilienė, "Analysis of the zero-crossing technique in relation to measurements of phase velocities of the Lamb waves," *Ultragarsas" Ultrasound",* vol. 65, pp. 7-12, 2010.

[24] D. Hutchins, K. Lundgren, and S. Palmer, "A laser study of transient Lamb waves in thin materials," *The Journal of the Acoustical Society of America,* vol. 85, pp. 1441-1448, 1989.

[25] N. A. Schumacher, C. P. Burger, and P. H. Gien, "A laser-based investigation of higher-order modes in transient Lamb waves," *The Journal of the Acoustical Society of America,* vol. 93, pp. 2981-2984, 1993.

[26] H. Nishino, T. Tanaka, K. Yoshida, and J. Takatsubo, "Simultaneous measurement of the phase and group velocities of Lamb waves in a laser-generation based imaging method," *Ultrasonics,* vol. 52, pp. 530-535, 2012/04/01/ 2012.

[27] J. E. Michaels, "Ultrasonic wavefield imaging: Research tool or emerging NDE method?," *AIP Conference Proceedings,* vol. 1806, p. 020001, 2017.

[28] D. Alleyne and P. Cawley, "A two-dimensional Fourier transform method for the measurement of propagating multimode signals," *The Journal of the Acoustical Society of America,* vol. 89, pp. 1159-1168, 1991.

[29] C.-H. Yeh and C.-H. Yang, "Characterization of mechanical and geometrical properties of a tube with axial and circumferential guided waves," *Ultrasonics,* vol. 51, pp. 472-479, 2011.

[30] M. Harb and F. Yuan, "A rapid, fully non-contact, hybrid system for generating Lamb wave dispersion curves," *Ultrasonics,* vol. 61, pp. 62-70, 2015.

[31] C.-M. Wu and Y.-C. Chen, "Statistical feature matrix for texture analysis," *CVGIP: Graphical Models and Image Processing,* vol. 54, pp. 407-419, 1992/09/01/ 1992.

[32] B. M. Asl and A. Mahloojifar, "A low-complexity adaptive beamformer for ultrasound imaging using structured covariance matrix," *IEEE Transactions on Ultrasonics, Ferroelectrics, and Frequency Control,* vol. 59, pp. 660-667, 2012.

[33] J. Takatsubo, B. Wang, H. Tsuda, and N. Toyama, "Generation Laser Scanning Method for the Visualization of Ultrasounds Propagating on a 3-D Object with an Arbitrary Shape," *Journal of Solid Mechanics and Materials Engineering,* vol. 1, pp. 1405-1411, 2007.